Stably stratified exact coherent structures in shear flow: the effect of Prandtl number

SCHOLARONE™
Manuscripts

Stably stratified exact coherent structures in shear flow: the effect of Prandtl number

Jake Langham[1]†, Tom S. Eaves[2] and Rich R. Kerswell[1,3]

[1]School of Mathematics, University of Bristol, Bristol, BS8 1TW, UK

[2]Department of Mathematics, University of British Columbia, 1984 Mathematics Rd., Vancouver, BC, V6T 1Z2, Canada

[3]Centre for Mathematical Sciences, University of Cambridge, Cambridge, CB3 0WA, UK

We examine how known unstable equilibria of the Navier-Stokes equations in plane Couette flow adapt to the presence of an imposed stable density difference between the two boundaries for varying values of the Prandtl number Pr, the ratio of viscosity to density diffusivity, and fixed moderate Reynolds number, $Re = 400$. In the two asymptotic limits $Pr \to 0$ and $Pr \to \infty$, it is found that such solutions exist at arbitrarily high bulk stratification but for different physical reasons. In the $Pr \to 0$ limit, density variations away from a constant stable density gradient become vanishingly small as diffusion of density dominates over advection, allowing equilibria to exist for bulk Richardson number $Ri_b \lesssim O(Re^{-2}Pr^{-1})$. Alternatively, at high Prandtl numbers, density becomes homogenised in the interior by the dominant advection which creates strongly stable stratified boundary layers that recede into the wall as $Pr \to \infty$. In this scenario, the density stratification and the flow essentially decouple, thereby mitigating the effect of increasing Ri_b. An asymptotic analysis is presented in the passive scalar regime $Ri_b \lesssim O(Re^{-2})$, which reveals $O(Pr^{-1/3})$-thick stratified boundary layers with $O(Pr^{-2/9})$-wide eruptions, giving rise to density fingers of $O(Pr^{-1/9})$ length and $O(Pr^{-4/9})$ width that invade an otherwise homogeneous interior. Finally, increasing Re to 10^5 in this regime reveals that *interior* stably stratified density layers can form away from the boundaries, separating well-mixed regions.

1. Introduction

The identification of numerous unstable invariant solutions in canonical shear flows has played a key role in the modern understanding of transitionally turbulent fluids. These states, most commonly known as *exact coherent structures (ECS)* underpin a deterministic picture of turbulence in which the flow is viewed as a complicated trajectory through a state space of velocity fields that satisfy the Navier-Stokes equations (Kerswell 2005; Eckhardt *et al.* 2007; Kawahara *et al.* 2012). The ECS are simple invariant solutions, equilibria, travelling waves and (relative) periodic orbits, that organise this state space through their stable and unstable manifolds. Though their unstable eigendirections prohibit them from being physically realised, turbulent flows may pass nearby to them. Consequently, the dynamical influence of ECS on the flow via their invariant manifolds is experimentally observable (Suri *et al.* 2017, 2018) and may be investigated in detail by high-resolution direct numerical simulations (DNS) (Kerswell & Tutty 2007; Gibson *et al.* 2008; Cvitanović & Gibson 2010; Budanur *et al.* 2017). As such, they have proven useful in investigating both the route to turbulence (Itano & Toh 2001; Skufca *et al.* 2006; Schneider *et al.* 2007; Kerswell & Tutty 2007; Viswanath & Cvitanović 2009; Mellibovsky *et al.* 2009; Schneider *et al.* 2010; Duguet *et al.* 2010; Pringle *et al.* 2012) and its subsequent features (Gibson *et al.*

† Email address for correspondence: j.langham@bristol.ac.uk

2008; Willis *et al.* 2013; Chandler & Kerswell 2013; Lucas & Kerswell 2015; Budanur *et al.* 2017).

Past work has focussed largely on understanding ECS in simple shear flows in channels and pipes whose physics can be parametrised by a single dimensionless variable: the Reynolds number Re. However, it is common in industrial, environmental and astrophysical flows, for the fluid to be subject to additional (buoyancy) forces due to gradients in density or temperature. In order to understand the role of ECS in such flows, one must therefore catalogue the effect of introducing this extra physics onto these states in homogeneous shear flows. Stratified flows require that at least two additional parameters be accounted for; the bulk Richardson number Ri_b controls the global level of stratification and the Prandtl number Pr sets the ratio of viscosity to density diffusion. While identifying ECS within this augmented parameter space presents a sizeable challenge, it is also an opportunity, since many physically relevant regimes remain unexplored.

A number of prior studies have investigated ECS in the stably stratified setting , where the bulk density gradient acts to suppress energetically unfavourable vertical motions. Eaves & Caulfield (2015) considered the effect of weak stratification on a particular state lying on the laminar-turbulent boundary in stratified plane Couette flow, providing a scaling argument which predicted that the usual physical structure of ECS (the SSP/VWI mechanism, see §2.2 and Waleffe 1997; Hall & Smith 1991; Hall & Sherwin 2010) is disrupted when $Ri_b = O(Re^{-2})$. This was subsequently confirmed asymptotically by both Deguchi (2017) and Olvera & Kerswell (2017). The latter study conducted a substantial survey of the Re-Ri_b space for plane Couette flows and $Pr = 1$, continuing solution branches for states at $Ri_b > 0$ that connect known unstratified ECS pairs, which can then be tracked into $Ri_b < 0$ (unstable stratification), to bifurcations of sheared Rayleigh-Bénard solutions. They noted that a key effect of increasing stratification is to encourage ECS to localise in one or more directions, conjecturing the existence of fully-localised states when $Ri_b = O(Re^0)$. Finally, Lucas *et al.* discovered ECS in stratified shear flow with a sinusoidal body forcing (Kolmogorov flow). They observed that both equilibria and turbulent DNS form shear and density layers originating from a sequence of linear 'zig-zag' instabilities in the (sinusoidal) base flow (Lucas *et al.* 2017), and converged periodic orbits to study how stratification affects mixing efficiency (Lucas & Caulfield 2017).

Despite this recent progress in the understanding of stratified ECS, a connection with realistic fully turbulent stratified shear flow remains unresolved (though Lucas *et al.* (2018) arguably see traces of underlying ECS in recent stratified plane Couette DNS results). In part this is due to the Prandtl number; prior stratified ECS studies have only dealt with unit Prandtl numbers (Eaves & Caulfield 2015; Deguchi 2017; Olvera & Kerswell 2017; Lucas *et al.* 2017; Lucas & Caulfield 2017) and full DNS of stratified shear flow turbulence is restricted in the Prandtl numbers it can access by issues of numerical resolution. However, Prandtl numbers observed in nature span a substantial range of scales, from as low as 10^{-7} (inside stars) to up to at least 10^{23} (Earth's mantle). On a more terrestrial level, temperature in air exhibits a Prandtl number around 0.7 (which is certainly attainable via DNS), whereas salt in water has $Pr \approx 700$ (currently unattainable via DNS, save in the $Ri_b \to 0$ limit).

This latter case of saltwater shear flow turbulence is of particular interest since the structure of turbulence in the oceans governs the mass transport across its depth (Munk 1966). As such, significant effort has been put into explaining the mass transport via modelling of the mixing of the density field that the turbulence causes (Linden 1979; Caulfield & Peltier 2003; Sutherland *et al.* 2019). Additionally, it has been observed that stratified shear flow turbulence typically organises into well-mixed constant density layers of large vertical extent separated by relatively thin interfacial regions between each layer (Turner 1973; Gregg 1980). Layers may appear spontaneously at turbulent Reynolds numbers and have been reproduced in a number of singly-diffusive experimental flows (Ruddick *et al.* 1989; Park *et al.* 1994; Holford & Linden 1999;

Oglethorpe *et al.* 2013; Thorpe 2016). (The doubly-diffusive case is also important, but beyond our scope.) The vertical extent of the well-mixed regions is linked to the flow speed and the buoyancy frequency (Thorpe 2016), but the detailed structure of the layers and the interfaces between them remains an open question, although the 'sharpness' of the interfaces appears to increase as the Prandtl number increases (Zhou *et al.* 2017b).

Low Prandtl number turbulence is less extensively studied, since fluids with high thermal diffusivities, such as molten metals, are typically difficult to deal with experimentally. However, turbulence arising from shear instabilities in low-*Pr* flows is hypothesised to significantly contribute to the chemical mixing processes within stellar radiation zones (Zahn 1992). Consequently, the value of examining (via analysis and DNS) simple shear flows in this limit has been recognised (Prat & Lignières 2013; Prat *et al.* 2016; Garaud *et al.* 2017).

Drawing motivation from the above examples and the recent interest in stratified ECS, our plan here is to complement the stratified plane Couette flow study of Olvera & Kerswell (2017), by probing the Ri_b-Pr space at fixed Reynolds number. We are particularly interested here in the as-yet unexplored limits $Pr \ll 1$ and $Pr \gg 1$, which are relevant for understanding astrophysical and geophysical flows respectively. The key questions are: (*a*) how strong can the bulk stratification be for ECS still to exist; and (*b*) what is the effect of *Pr* on the structure of solutions? The outline of the paper is as follows. In §2, we detail the physical system, the numerical methods used and the necessary underlying theory (SSP/VWI) for exact coherent states in shear flows. We then take the principal solution of Olvera & Kerswell (2017) and perform parameter continuation in Ri_b for a wide range of fixed Prandtl numbers (§3), allowing us to identify the range of global stratification that states exist for, before splitting our analysis into the low-*Pr* (§3.1) and high-*Pr* (§3.2) limits. In the low-*Pr* case, we identify and study an asymptotic solution branch onto which all states collapse. For high-*Pr* states, we intriguingly observe the density field splitting into a homogenised region with highly stratified boundary layers at the walls, punctuated by jets of advected density. We conduct an analysis in §3.2.1 of its structure in the limit of weak stratification, before proceeding in §3.2.2 to consider increasing Ri_b. As states leave the weakly stratified regime, their velocity perturbations retreat from the walls, apparently inhibited by the presence of high stratification. Section 4 concludes with a final discussion of these results and presents some preliminary observations of interfaces developing in the channel interior as *Pr* increases at high Reynolds number.

2. Setting

2.1. *Stratified plane Couette flow*

The setting for this study is plane Couette flow, which is the flow of an incompressible viscous fluid between two infinite parallel plates at $y = \pm h$, moving with velocities $\pm U e_x$. The flow velocity is represented as $\boldsymbol{u} := u e_x + v e_y + w e_z$ (where e_x, e_y and e_z indicate the *streamwise*, *wall-normal* and *spanwise* directions respectively) and obeys no-slip boundary conditions at the plates. Gravity is taken to act in the wall-normal direction, $\boldsymbol{g} = -g e_y$. Fixed, but differing densities $\rho_0 \mp \Delta_\rho$ are imposed at the plates $y = \pm h$, where $\Delta_\rho \ll \rho_0$ so the Boussinesq approximation can be used. The governing equations for the fluid velocity $\boldsymbol{u}$, pressure p and density ρ are

$$\frac{\partial \boldsymbol{u}}{\partial t} + \boldsymbol{u} \cdot \boldsymbol{\nabla} \boldsymbol{u} = -\boldsymbol{\nabla} p + \frac{1}{Re} \nabla^2 \boldsymbol{u} - Ri_b \rho \, \boldsymbol{e}_y, \tag{2.1a}$$

$$\boldsymbol{\nabla} \cdot \boldsymbol{u} = 0, \tag{2.1b}$$

$$\frac{\partial \rho}{\partial t} + \boldsymbol{u} \cdot \boldsymbol{\nabla} \rho = \frac{1}{RePr} \nabla^2 \rho, \tag{2.1c}$$

where U, h and Δ_ρ, have been used to non-dimensionalise the system (so that the total dimensional density is $\rho_0 + \Delta_\rho \rho$, for example). The dimensionless parameters Re, Pr and Ri_b are the *Reynolds*, *Prandtl* and *bulk Richardson* numbers respectively, defined as

$$Re := \frac{Uh}{\nu}, \quad Pr := \frac{\nu}{\kappa}, \quad Ri_b := \frac{\Delta_\rho}{\rho_0} \frac{gh}{U^2}, \tag{2.2}$$

where ν is the kinematic viscosity of the fluid and κ is the diffusivity of some density-affecting agent, such as temperature or salt content. The accompanying boundary conditions are $u = \pm 1$, $v = 0$, $w = 0$, $\rho = \mp 1$ at the walls $y = \pm 1$ which, along with Eqs. (2.1a)–(2.1c), admit a steady base flow with linear velocity and density profiles:

$$\boldsymbol{u} = y\boldsymbol{e}_x, \quad p = Ri_b y^2/2, \quad \rho = -y. \tag{2.3}$$

2.2. *SSP/VWI mechanism*

In this study, we analyse unstable equilibrium solutions to Eqs. (2.1a)–(2.1c) that differ from the basic laminar flow. Almost all such states in homogeneous shear flows where the laminar base state is linearly stable arise physically due to the *self-sustaining process (SSP)* mechanism proposed by Waleffe (1997), which was subsequently recognised to be the finite-Re manifestation of the *vortex-wave-interaction (VWI)* theory (Hall & Smith 1991; Hall & Sherwin 2010). (The state proposed by Smith & Bodonyi (1982) and recently found numerically by Deguchi & Walton (2013) is one exception.)

The SSP/VWI process relies on three flow structures, *rolls, streaks* and *waves*, sustaining each other against dissipation in a closed loop. Streamwise rolls advect the underlying shear causing the streamwise velocity to vary in the spanwise direction, thereby creating *streaks*, sustained patches of negative or positive streamwise velocity adjustments to the basic shear. If these streaks have large enough amplitude, they are unstable to streamwise-varying waves, which, via the quadratic nonlinearity in Eq. (2.1a), can then energise the original streamwise rolls to close the loop. This process is covered in great detail elsewhere (Hamilton *et al.* 1995; Waleffe 1997; Hall & Smith 1991; Hall & Sherwin 2010). At asymptotically high Reynolds number, these states have the following structure:

$$u = \quad \bar{u}(y,z) + \ldots + \delta'(Re)[U(y,z)e^{ikx} + \text{c.c.}] + \ldots \tag{2.4a}$$

$$v = Re^{-1}\bar{v}(y,z) + \ldots + \delta'(Re)[V(y,z)e^{ikx} + \text{c.c.}] + \ldots \tag{2.4b}$$

$$w = Re^{-1}\bar{w}(y,z) + \ldots + \delta'(Re)[W(y,z)e^{ikx} + \text{c.c.}] + \ldots \tag{2.4c}$$

$$p = Re^{-2}\bar{p}(y,z) + \ldots + \delta'(Re)[P(y,z)e^{ikx} + \text{c.c.}] + \ldots \tag{2.4d}$$

where $\delta'(Re) = Re^{-7/6}$, except in the $O(Re^{-1/3})$-thick critical layer (located where the laminar base flow vanishes for equilibria), where it is $Re^{-5/6}$ (Hall & Sherwin 2010). Here,

$$\bar{q} := \frac{1}{L_x}\int_0^{L_x} q\, \mathrm{d}x \tag{2.5}$$

denotes the streamwise average of a given flow field q. In these expressions, $(\bar{u}, 0, 0)$ represents the streak-modified base shear, $(0, \bar{v}, \bar{w})$ the streamwise rolls and (U, V, W) the amplitudes of the streamwise-varying wave field.

Although strictly valid only in the high-Re limit, VWI captures the physics of SSP remarkably well, all the way down to transitionally turbulent Re (Hall & Sherwin 2010), which is the regime considered in the bulk of this study. The theory has been extended in the stratified setting by Hall (2012), to incorporate plane Couette flows with a buoyancy force aligned with the streamwise direction. Later, Deguchi (2017) and Olvera & Kerswell (2017) considered the vortex-wave interaction for the situation herein with buoyancy in the wall-normal direction,

presenting numerical calculations at varying *Re* and fixed *Pr* = 1. In this study, we use the VWI scalings in Eqs. (2.4*a*)–(2.4*d*) to look at the effect of varying *Pr* on states at fixed *Re*.

2.3. *Numerical methods*

The numerical solutions presented below were obtained primarily using a bespoke pseudo-spectral code that computes steady solutions of Eqs. (2.1*a*)–(2.1*c*), in the box $(x, y, z) \in [0, L_x] \times [-1, 1] \times [0, L_z]$, with periodic streamwise and spanwise directions of lengths L_x and L_z respectively. The standard Newton-Raphson method was used to converge equilibria, with LU decomposition to invert the full discretised system Jacobian.

The additional solutions in §3.2.3 were obtained using a modified version of the Channelflow 2.0 DNS software (Gibson *et al.* 2019) that employs a matrix-free iterative solver to find invariant solutions via two standard methods: Stokes preconditioning (Tuckerman 1989) and time integration (Viswanath 2007; Gibson *et al.* 2008). The former method was used to the compute $Pr \lesssim 10$ solutions in §3.2.3 and the latter was used at higher *Pr*, where the Stokes-preconditioned system suffers the effects of poorer numerical conditioning more acutely (Tuckerman *et al.* 2019).

Provided enough computer memory is available, we find that our bespoke solver is typically preferable to the standard iterative schemes. The reason is twofold: firstly, there is no need to perform multiple expensive time integrations to compute states. (Though we note that the recent parallelisation of the Channelflow code, see Gibson *et al.* (2019), has made time integration much more attractive, paving the way for fast ECS computations with very high spatial resolutions.) Secondly, we restrict solutions to a highly-symmetric subspace, thereby reducing the size of the basis set needed to represent the states at a given spatial resolution and substantially decreasing the cost of an exact matrix inversion. See Appendix A for technical details. Following the previous work (Deguchi 2017; Olvera & Kerswell 2017), the symmetries imposed (in addition to L_x- and L_z-periodicity) are: 'shift-and-reflect' $\mathcal{S}$, rotation about the *z*-axis Ω and spanwise reflection $\mathcal{Z}$, defined by

$$\mathcal{S} : [u, v, w, p, \rho](x, y, z) \mapsto [u, v, -w, p, \rho](x + L_x/2, y, L_z/2 - z), \quad (2.6a)$$

$$\Omega : [u, v, w, p, \rho](x, y, z) \mapsto [-u, -v, w, p, -\rho](-x, -y, z), \quad (2.6b)$$

$$\mathcal{Z} : [u, v, w, p, \rho](x, y, z) \mapsto [u, v, -w, p, \rho](x, y, -z). \quad (2.6c)$$

Below, streamwise-averaged quantities will often be plotted which, because of $\mathcal{S}$, possess an additional spanwise reflection symmetry in the line $z = \pi/4$. This implies that the cells $[-1, 1] \times [0, L_z/2]$ and $[-1, 1] \times [L_z/2, L_z]$ are identical and obey reflection symmetries along the lines $z = \pi/4$ and $z = 3\pi/4$ respectively.

The majority of the results presented involve a single $\mathcal{S}$-, Ω- and $\mathcal{Z}$-symmetric solution family described at the beginning of §3 and were computed with the direct solver in a domain with $L_x = 2\pi$ and $L_z = \pi$, at *Re* = 400. Channelflow was later employed to obtain the additional §3.2.3 equilibria in a box with $L_x = 2\pi/1.14$, $L_z = 2\pi/2.5$, *Re* = 400 and to cross-check a sample of solutions from the direct solver. It is worth mentioning here, that in both cases, these results demanded very high numerical resolutions. Indeed, the §3.2 and §3.2.3 solutions at high Prandtl number may represent some of the most highly resolved ECS converged to date. Further details, including typical resolutions achieved are given in Appendix A.

Both codes are coupled to a pseudo-arclength continuation algorithm that enables straightforward computation of solution families parametrised by *Re*, Ri_b or *Pr*. This allows us to track solution curves which, for the ECS studied herein, arise via saddle-node bifurcations (Gibson *et al.* 2009) with distinct *upper* and *lower* branches. (The lower branch lies closest to the laminar base state in any reasonable metric, e.g. energy, dissipation, amplitude.) Since multiple equilibria
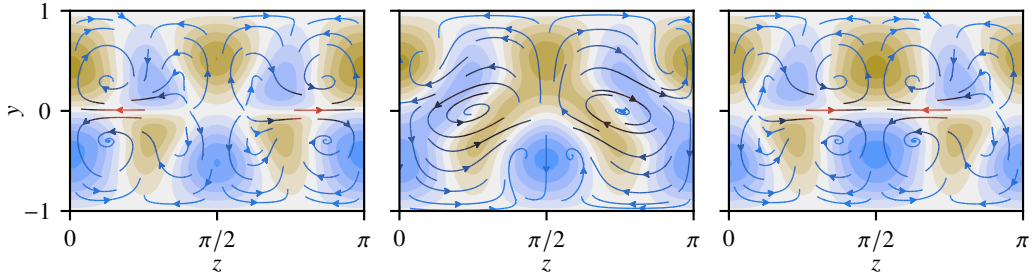
FIGURE 1. Spanwise cross-sections of the EQ_7 state at $Re = 400$ without stratification. The plots show the streamwise velocity perturbation $\hat{u} := u - y$, plotted using 11 equally-spaced contour intervals between -0.22 (brown) and 0.22 (blue). The middle interval is centred at zero (white). Overlaid are streamlines of the (v, w)-field, coloured with a linear gradient from blue to red according to the magnitude of in-plane velocity, which lies in the interval $[0, 0.077]$. Three (y, z)-slices are given, at $x = 0$, $x = \pi/2$ and $x = \pi$ (left to right), covering half the computational domain.

may exist at the same point in parameter space, we use the 'surplus' mean wall stress

$$\tau_y := \frac{1}{L_x L_z} \int_0^{L_x} \int_0^{L_z} \left. \frac{\partial u}{\partial y} \right|_{y=1} \mathrm{d}x \, \mathrm{d}z - 1, \tag{2.7}$$

to distinguish between them (where $\tau_y = 0$ for the base flow).

3. Results

This study focusses mainly on a lower branch equilibrium solution originally discovered by Itano & Generalis (2009), who computed it via homotopy from a solution in an unstably stratified channel with stationary walls and Gibson *et al.* (2009), who independently converged it from snapshots of a transitionally turbulent flow simulation. We follow the nomenclature used by Gibson *et al.* (2009), whose search identified 13 different equilibria and named them EQ_1–EQ_{13}. Our chosen solution is EQ_7 and its upper branch counterpart EQ_8. In the vertically stratified case with $Pr = 1$, EQ_7 was recently studied by Olvera & Kerswell (2017), who observed that it lies on the so-called *edge manifold* separating laminar and turbulent dynamics and is therefore likely to play a role in organising the transition process. In §3.2.3 we briefly address other equilibrium solutions.

Figure 1 shows yz-contours of the perturbation to the laminar base flow $\hat{u} := u - y$, for EQ_7 with no imposed stratification. Also shown are (v, w)-streamlines, coloured from blue to red according to the speed of the flow in the plane. The leftmost panel is a slice through $x = 0$. It contains two rows of four streaks, separated by the centre line $y = 0$. The in-plane streamlines provide insight into the formation of the streaks. For example, the negative (brown) streak centred at approximately $(z, y) = (\pi/4, -0.5)$ arises due to uplift of negative streamwise velocity from the laminar base flow near the lower wall. Likewise, the other streaks emerge at regions of inflow and outflow from the boundaries, with the strongest in-plane advection accounting for the largest streaks, centred along the line $z = 0 \equiv \pi$. In the middle panel at $x = \pi/2$, there is transport between the upper and lower half-channels due to vortices centred at $(\pi/4, 0)$ and $(3\pi/4, 0)$ and some of the streaks have merged into larger structures. The final panel at $x = \pi = L_x/2$ is dictated by the imposed symmetries (specifically $\mathcal{S}$ and $\mathcal{Z}$), which constrain it to be equal to an $L_z/2$-spanwise shift of the $x = 0$ slice. Likewise, the remainder of the the computational domain, $\pi < x \leqslant 2\pi$, is determined this way. Slices at intermediate streamwise co-ordinates gradually interpolate between the panels shown and all the states considered herein possess either a similar,
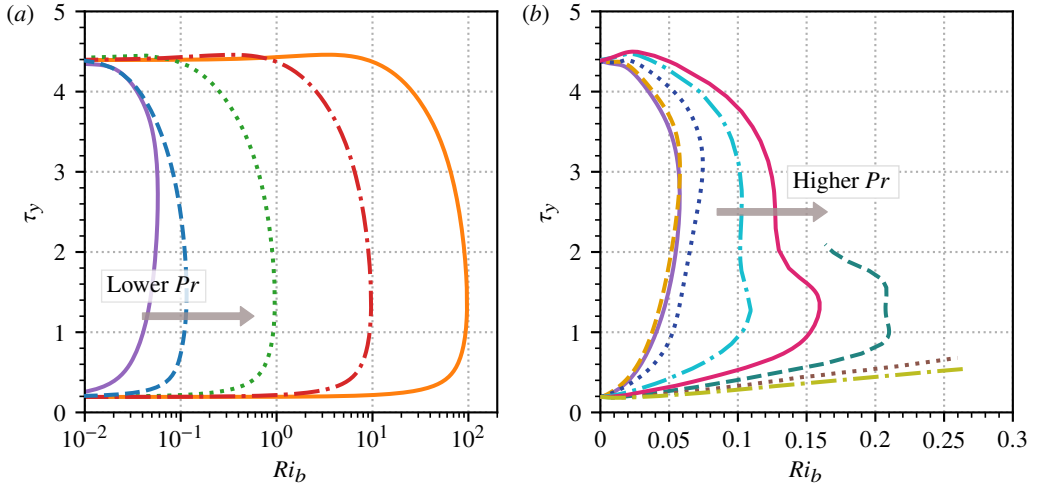
FIGURE 2. Parameter continuation curves for the EQ_7 (lower) / EQ_8 (upper) states in terms of the bulk Richardson number and mean wall stress τ_y for different Prandtl numbers. (*a*) Low-Pr states: $Pr = 10^0$ (purple solid), $Pr = 10^{-1}$ (blue dashed), $Pr = 10^{-2}$ (green dotted), $Pr = 10^{-3}$ (red dash-dot) and $Pr = 10^{-4}$ (orange solid). The bifurcation point of the $Pr = 10^{-4}$ curve is at $Ri_b \approx 97$. (*b*) Higher-Pr states: $Pr = 1$ (purple solid), 2 (yellow dashed), 7 (navy dotted), 20 (cyan dash-dot), 40 (magenta solid), 70 (teal dashed), 120 (brown dotted), 200 (olive dash-dot).

or lower level of streamwise variation. Therefore, in the following we only use slices at $x = 0$ and $\pi/2$ to visualise states or, more commonly take a streamwise average.

To examine how EQ_7 (and where possible, EQ_8) is affected by varying the Prandtl number, a pseudo-arclength continuation algorithm was used to converge states at fixed $Re = 400$ and varying Pr and Ri_b. Starting with initial parameters $Pr = 1$, $Ri_b = 0$, continuation was first performed on Pr in both directions to obtain solutions with a wide spread of Prandtl numbers ranging from $Pr = 10^{-4}$ to $Pr = 500$. The character of these states depends strongly on whether the Prandtl number is significantly less or greater than unity and we divide our study along these lines.

Figure 2 shows solution branches of the EQ_7 and EQ_8 states, obtained by starting with the states at $Pr = 10^{-4}$ to 200 and continuing them in Ri_b. Part (*a*) plots the continuation curves for $Pr \leqslant 1$. All five curves are similar, possessing the familiar shape of a saddle-node bifurcation. Starting from $Ri_b = 0$, both lower and upper branches enter an initial regime (present, but not shown for $Pr = 1$) where their mean wall stress is unaffected by the presence of global stratification. This is followed by a transition between solution branches where the stress changes comparatively rapidly. The range of admissible bulk Richardson numbers increases dramatically as Pr decreases, suggesting that in the limit of low Pr, ECS are insensitive to stratification and may persist up to arbitrarily high Ri_b as Pr is reduced.

Figure 2(*b*) shows the $Pr \geqslant 1$ continuation curves. The $Pr = 1$, 2 and 7 curves have essentially the same shape as the low-Pr curves. At higher Pr, the solution branches follow the opposite trend to the low-Pr case, reaching progressively higher Ri_b as the Prandtl number *increases*. Another trend to note is that the upper branches reach increasingly higher mean wall stresses than EQ_8 itself. The $Pr \geqslant 40$ curves required high numerical resolution to be continued reliably, for reasons which shall become clear in §3.2. The three highest Pr curves, which terminate before reaching EQ_8, were continued as far as available computational resources permitted, the final two not reaching their saddle-node bifurcations. Nevertheless, the $Pr = 70$, 120 and 200 curves persist up to at least $Ri_b = 0.21$, 0.26 and 0.27 respectively. This trend along the lower

branch suggests that EQ_7 might admit arbitrarily large global stratification in the high-Pr limit. We now analyse the solutions of Fig. 2 in the two defined limits.

3.1. *Low Prandtl number ($Pr \ll 1$)*

At low Pr, density transport in the fluid is diffusion dominated and as a result ρ should not develop small scales or deviate far from the basic state. To reflect at least the latter, we consider the expansion $\rho(x, y, z) = -y + \varepsilon\rho_1(x, y, z) + \ldots$, where ε is a small parameter to be determined, with $\rho_1 = O(Pr^0)$. This is certainly true at either end of the continuation curves in Fig. 2(a) where $Ri_b \to 0$, but will be found to be true over the whole curve. Working with the perturbations to the laminar base state $\hat{u} := u - y$, $\hat{v} := v$, $\hat{w} := w$, $\hat{p} := p - Ri_b y^2/2$ and $\hat{\rho} := \rho + y = \varepsilon\rho_1 + \ldots$, the steady form of Eq. (2.1c) becomes

$$\varepsilon(y + \hat{u})\frac{\partial\rho_1}{\partial x} + \hat{v}\left(-1 + \varepsilon\frac{\partial\rho_1}{\partial y}\right) + \varepsilon\hat{w}\frac{\partial\rho_1}{\partial z} = \frac{\varepsilon}{RePr}\nabla^2\rho_1, \tag{3.1}$$

after neglecting $O(\varepsilon^2)$ terms. We now determine the leading-order velocity fields in Eq. (3.1) from the asymptotic VWI structure in Eqs. (2.4a)–(2.4d). The cross-stream velocity $\hat{v}$ is largest for the wave field in the critical layer, but because of the enhanced gradients of $O(Re^{1/3})$ across this region, this flow actually drives a smaller density field of $O(\varepsilon Re^{-1/2})$ than the streamwise rolls outside the critical layer, which drive an $O(\varepsilon)$ density field. Therefore, the leading order physics is away from the critical layer, so that $\hat{v} = \bar{v}(y, z)/Re$ and $\hat{w} = \bar{w}(y, z)/Re$ and Eq. (3.1) can be rewritten as

$$\bar{v}\left(-1 + \varepsilon\frac{\partial\rho_1}{\partial y}\right) + \varepsilon\bar{w}\frac{\partial\rho_1}{\partial z} = \frac{\varepsilon}{Pr}\nabla^2\rho_1, \tag{3.2}$$

where, because the driving term is streamwise-independent, $\rho_1 = \rho_1(y, z)$ and the streamwise advection term drops. This then leads to $\varepsilon = Pr \ll 1$ and the leading equation

$$-\bar{v} = \nabla^2\rho_1. \tag{3.3}$$

Inverting this relationship, the leading density perturbation $\hat{\rho} = -RePr\Delta^{-1}\hat{v}$ (where $\Delta := \nabla^2$) can then be eliminated from the Navier-Stokes equations to leave the low-Pr equations (or low-Péclet number equations, see Lignières 1999):

$$(y + \hat{u})\hat{u}_x + \hat{v}\left(1 + \hat{u}_y\right) + \hat{w}\hat{u}_z + \hat{p}_x = Re^{-1}\nabla^2\hat{u}, \tag{3.4a}$$

$$(y + \hat{u})\hat{v}_x + \hat{v}\hat{v}_y + \hat{w}\hat{v}_z + \hat{p}_y = Re^{-1}\left[\nabla^2 + Ri_b PrRe^2\Delta^{-1}\right]\hat{v}, \tag{3.4b}$$

$$(y + \hat{u})\hat{w}_x + \hat{v}\hat{w}_y + \hat{w}\hat{w}_z + \hat{p}_z = Re^{-1}\nabla^2\hat{w}, \tag{3.4c}$$

$$\hat{u}_x + \hat{v}_y + \hat{w}_z = 0. \tag{3.4d}$$

This makes it clear that solutions can only depend on the Richardson number Ri_b and the Prandtl number Pr in the combination $Ri_b Pr$. Furthermore, the cross-stream momentum equation, Eq. (3.4b), also implies that there exists a region of weakly stratified (small Ri_b) flow where the Navier-Stokes and the density equations remain effectively uncoupled until $Ri_b = O(Pr^{-1}Re^{-2})$. These are the flat regions of both the upper and lower solution branches in Fig. 2(a), where increasing Ri_b has no effect on τ_y. As $Pr \to 0$, these regions extend to $Ri_b \sim O(1/Pr)$.

This scaling result, $Ri_b = O(Pr^{-1}Re^{-2})$, equivalent to the Rayleigh number $Ra := -Ri_b PrRe^2$ being $O(1)$, was first observed numerically in the $Pr = 1$ case by Eaves & Caulfield (2015) and then in the analysis of Deguchi (2017) and Olvera & Kerswell (2017). There, at least for $Pr = O(1)$, once the stratification strength increases beyond this scaling, new dynamic balances emerge [e.g. 'regime 2' in Olvera & Kerswell (2017), ultimately followed by the 'unit Reynolds number Navier-Stokes' (UNS) regime of Deguchi (2017) or 'regime 3' of Olvera & Kerswell
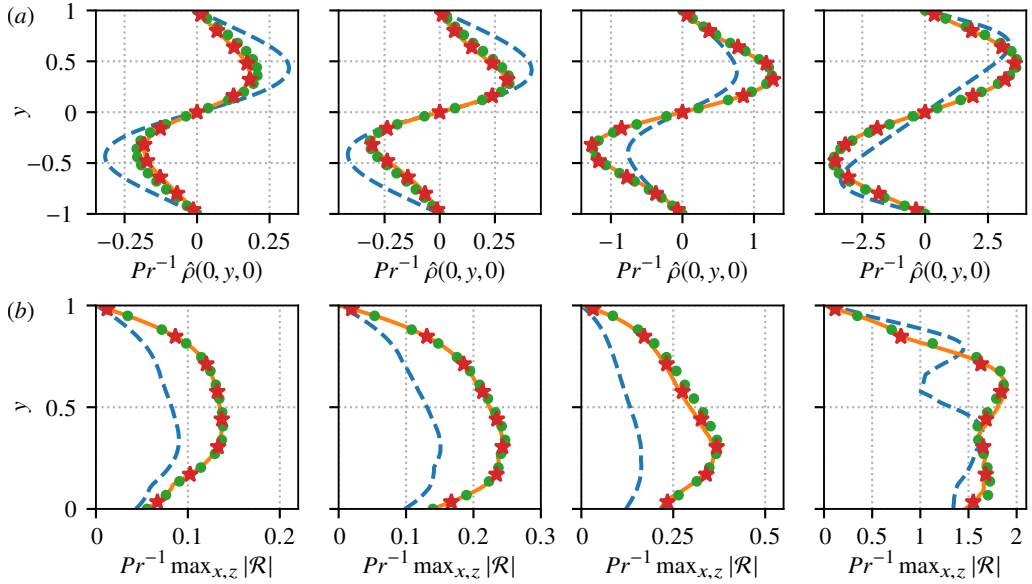
FIGURE 3. Verification of the $O(Pr)$ scalings predicted for low Prandtl number ECS. In all plots the Prandtl numbers are $Pr = 10^{-1}$ (blue dashed), $Pr = 10^{-2}$ (green circles) $Pr = 10^{-3}$ (red stars) and $Pr = 10^{-4}$ (orange solid). Across each column $PrRi_b$ is fixed at a given point along the solution curves plotted in Fig. 4(a). From left to right: $PrRi_b = 0$, 0.005 (lower branch), 0.097 (saddle-node) and 0.005 (upper branch). (a) Cross-channel profiles of $\hat{\rho}$, for $x, z = 0$, rescaled by Pr^{-1}. (b) Absolute maximum values along streamwise and spanwise directions of $\mathcal{R} := \hat{v} + \nabla^2 \hat{\rho}/(RePr)$, rescaled by Pr^{-1}.

(2017)]. Here however, in the $Pr \to 0$ limit this is not the case. In Fig. 3(a), we demonstrate that the $O(Pr)$ scaling of the density perturbation persists along the *whole* length of the solution curves. The leftmost figure verifies the situation for EQ_7 at $Ri_b = 0$ (where the stratification is still present but the buoyancy force is switched off), plotting $Pr^{-1}\hat{\rho}$ as a function of y for $x, z = 0$. These slices, taken from solutions at $Pr = 10^{-1}, 10^{-2}, 10^{-3}$ and 10^{-4}, collapse neatly onto an asymptotic profile for $Pr \gtrsim 10^{-2}$. The subsequent plots confirm that the same holds for $Ri_b > 0$ solutions using the same Prandtl numbers, at various points along the solution branches, now keeping the size of the buoyancy forcing constant. This property is not specific to our choice of $x, z = 0$. We have checked that the scalings are observed for profiles with $x = 0, \pi/4, \pi/2, 3\pi/4$ and $z = 0, \pi/2$.

In Fig. 3(b), we plot $\max_{x,z} |\hat{v} + \nabla^2 \hat{\rho}/(RePr)|$ at the same points along the solution curves as in Fig. 3(a). These curves collapse upon rescaling by Pr^{-1}, confirming that Eq. (3.3) is obeyed up to an $O(\varepsilon)$ error term across the whole domain, as implied by Eq. (3.2). The conclusion is then that solutions should be self-similar in the limit of low Pr along the whole solution curve. Figure 4(a) replots the parameter continuation curves in Fig. 2(a) against $Ri_b Pr$, confirming the collapse onto a single asymptotic branch. In particular, this implies that the maximum bulk Richardson number for these solutions is $Ri_b^m \approx 0.01/Pr$ at $Re = 400$ as $Pr \to 0$.

In Fig. 4(b) we plot contour slices through the yz-plane along the $Pr = 10^{-4}$ curve. The contour plots are organised in numbered side-by-side pairs, showing streamwise averages of $\hat{u}$ on the left and $\hat{\rho}$ on the right. Along the lower branch (plots 1–3) we see that the streaks centred at $z = \pi/4$ and $3\pi/4$ shrink as Ri_b increases. At the saddle-node (plot 4) they have disappeared completely and the mean $\hat{u}$ field becomes separated into negative (upper) and positive (lower) halves. This can be traced to the $\hat{v}$ field, which feeds these streaks by advecting the base shear; its streamwise average is plotted in Fig. 5. (For reference, the corresponding roll streamlines are included in
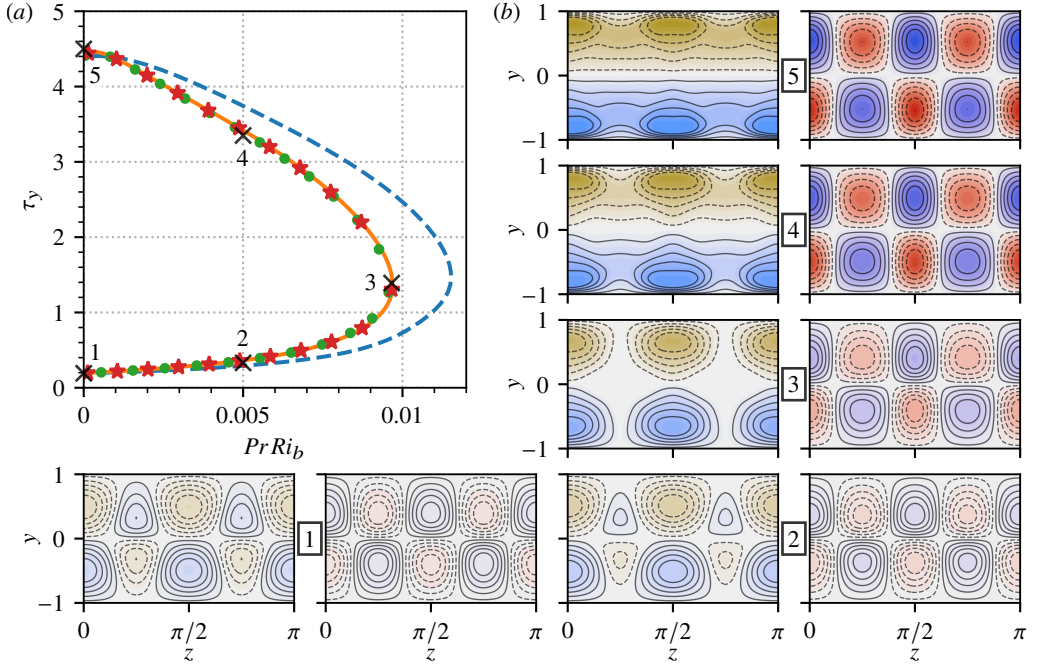
FIGURE 4. Self-similar solution branches of EQ_7 (lower) / EQ_8 (upper) in the $Pr \to 0$ limit. (*a*) Parameter continuation curves in bulk Richardson number as a function of mean wall stress. The horizontal axis has been rescaled by Pr causing the curves to collapse. The Prandtl numbers match those in Fig. 3. (*b*) Pairs of contour plots along the $Pr = 10^{-4}$ branch (orange solid), numbered according to the labelled points in part (*a*). Lefthand plots show the streamwise average of $\hat{u}$, shaded between -0.8 (brown) and 0.8 (blue). Righthand plots show the streamwise average of the $\hat{\rho}$ field, shaded between -2.3×10^{-4} (red) and 2.3×10^{-4} (blue). In all plots, the middle contour interval is white and centred at zero; black contour lines are overlaid to show the structure of solutions, using 11 equally spaced intervals, between $\pm \max_{y,z} |\bar{u} - y|$ or $\pm \max_{y,z} |\bar{\rho}|$ for each field, as appropriate. Dashed lines are negative contours and solid lines are positive. Anti-clockwise from bottom left: $PrRi_b = 0$ (EQ_7, point 1), 0.005 (point 2), 0.097 (saddle-node, point 3), 0.005 (point 4), 0 (EQ_8, point 5).
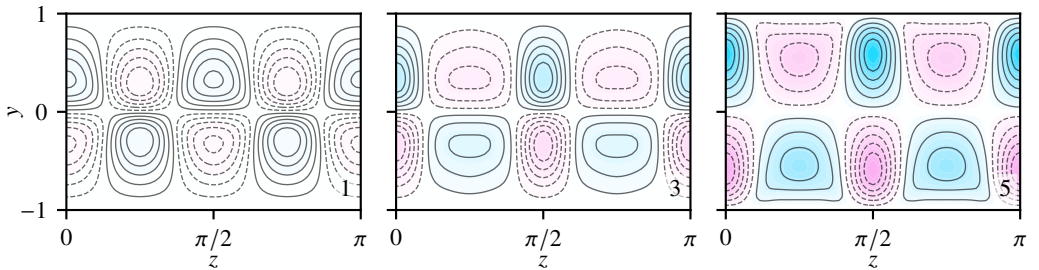

FIGURE 5. Contour plots of $\bar{v}(y, z)$ along the $Pr = 10^{-4}$ solution branch, at the numbered points indicated in Fig. 4(*a*): from left to right, the plots correspond to the first (EQ_7), third (saddle-node) and fifth (EQ_8) solution pairs in Fig. 4(*b*). The contours are shaded between -0.19 (pink) and 0.19 (cyan); black contour lines are overlaid using 11 equally spaced intervals, between $\pm \max_{y,z} |\bar{v}|$, which equals 0.014, 0.076 and 0.19 respectively. Dashed contours indicate $\bar{v} < 0$, solid contours $\bar{v} > 0$.
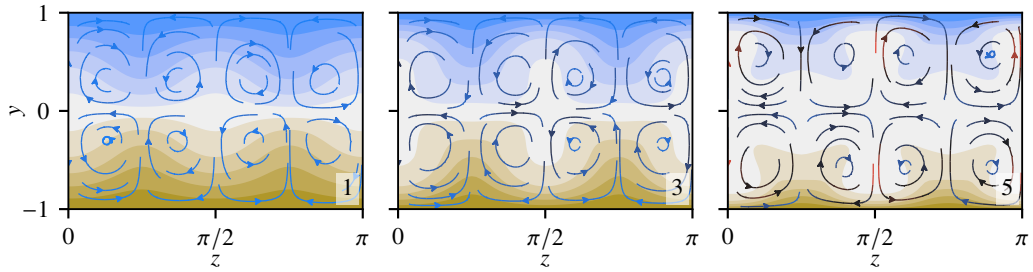
FIGURE 6. Contour plots of $\bar{u}(y, z)$ for $Pr = 10^{-4}$ solutions at the numbered points indicated on the solid orange Fig. 4(a) curve. From left to right, the plots correspond to the first (EQ_7), third (saddle-node) and fifth (EQ_8) plotted solutions in Fig. 4(b). Overlaid are $(\bar{v}, \bar{w})$-streamlines, coloured with a linear gradient from blue to black to red, according to $|(\bar{v}, \bar{w})|$, which lies in the interval $[0, 0.19)$.

Fig. 6.) As the state transitions from the less energetic EQ_7 state toward the more energetic EQ_8, the overall strength of the $\hat{v}$ field increases (as do the magnitudes of $\hat{u}$ and $\hat{\rho}$, which are driven by $\hat{v}$). However, the increased buoyancy force from point 1 to point 3 penalises upward motion wherever $\hat{\rho} > 0$ and downward motion where $\hat{\rho} < 0$. Consequently, there is a redistribution of the $\hat{v}$ field along the lower branch, diminishing in regions where the signs of $\hat{v}$ and $\hat{\rho}$ match (outflow from the walls) and concentrating where they differ (inflow to the walls). This leads to the (inflow) streaks centred at $z = 0 \equiv \pi$ and $\pi/2$ becoming increasingly dominant. This division persists along much of the upper branch, connecting through to the EQ_8 solution where the unevenly distributed wall-normal velocity field and corresponding streak structure exist in the unstratified setting.

The qualitative effect of these trends along the solution branches on the streamwise transport is shown in Figure 6, which shows the $\bar{u}$ field for EQ_7 at $Ri_b = 0$ (left plot), at the saddle-node (middle plot) and EQ_8 at $Ri_b = 0$ (right plot). This shows that by the end of the lower branch, $\hat{u}$ is large enough to cancel the base laminar shear flow solution in some regions (i.e. $u = y + \hat{u} = 0$). The overlaid streamlines highlight the underlying roll advection, its increasing significance and the uneven distribution of inflow versus outflow to the walls. However, it is important to note that while streamwise-averaged quantities indicate overall trends, the streamwise dependence observed in Fig. 1 is present and persists along the solution curves. Specifically, it is not the case that u is homogenised throughout the channel interior along the upper branch, even though this is true in a streamwise-averaged sense.

3.2. *High Prandtl number ($Pr \gg 1$)*

Just as in the case of low Prandtl number, solution curves calculated with large Pr access higher and higher bulk Richardson numbers as Pr increases. However, the mechanism which allows this is quite different, since $\hat{\rho}$ is no longer a weak perturbation of the uniform laminar density profile. In Fig. 7 we plot contour slices through the yz-plane at $x = 0$ (top row) and $\pi/2$ (bottom row) of the full density field ρ for $Pr = 1, 5$ and 20. The bulk Richardson number is 0.01 and the velocity field is near that of the (unstratified) lower-branch EQ_7 solution. Starting at $Pr = 1$ (leftmost column), the density field for $x = 0$ is a spanwise-wavy modulation of the laminar base profile. Centred at $z = 0$, there is a well-mixed region, where $\rho \approx 0$, sandwiched between two regions of strong spanwise inflow along the centreline $y = 0$. In the $\pi/2$ slice, in-plane advection is dominated by vortices centred at $(z, y) = (\pi/4, 0)$ and $(3\pi/4, 0)$, inducing a global spanwise wave. At $Pr = 5$ (middle column) the spanwise waviness in both x slices has become much more exaggerated, with peaks of extremal density advected towards $y = 0$ and corresponding troughs sent out towards the walls. In between these features, regions of approximately zero density are now well established. By $Pr = 20$ (rightmost column), the spanwise-wavy structures
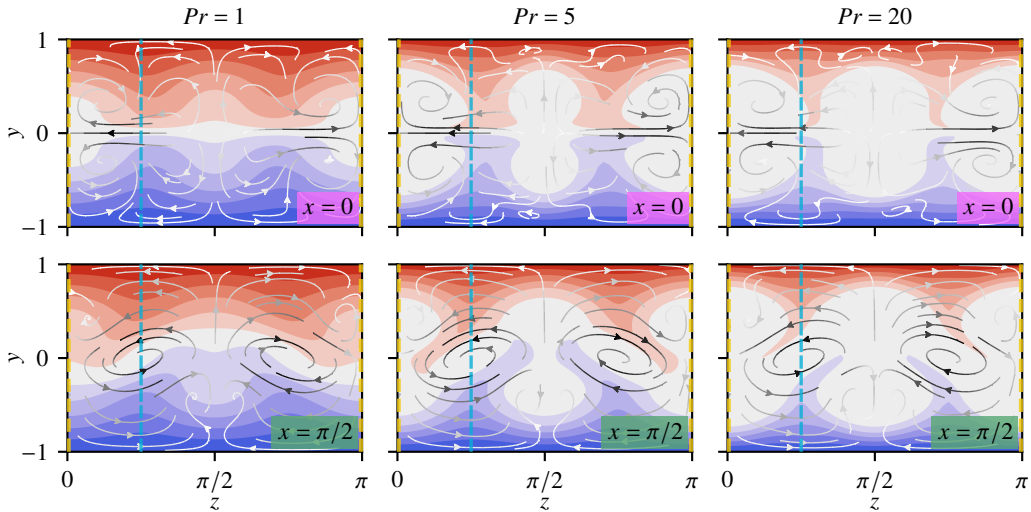
FIGURE 7. Contour plots of $\rho(x, y, z)$, through $x = 0$ (top row) and $x = \pi/2$ (bottom row) of the EQ_7 state at $Pr = 1$, 5 and 20 (left to right) and $Ri_b = 0.01$. Contours are equally spaced from -1 (red) to 1 (blue) with a width of 2/11, ensuring that the middle band (white) is centred at zero. Overlaid are (v, w)-streamlines, coloured with a linear gradient from white to black according to the magnitude of (v, w) across all six plots, which lies in the interval [0, 0.154]. The coloured dashed lines through $z = 0$ and $\pi/4$ indicate the locations of the contour slices plotted in Fig. 8.

have become spanwise localised 'finger'-like incursions into an otherwise uniformly dense and neutrally buoyant channel interior. Moreover, the regions in the vicinity of the walls have become highly stratified.

Figure 8 shows contour slices in the xy-plane using the same solutions as Fig. 7. In this case, the Prandtl number increases moving down each column. The left column is a slice through $z = 0$; we see that the interior in this region is already homogenised by $Pr = 5$ across the full length of the channel. The righthand column is a slice through $z = \pi/4$. Even in this region, by $Pr = 20$, the interior appears to be homogenising, despite the aforementioned inflow of density from the walls.

At the channel walls, the homogenising density profile must connect to $\rho(x, \pm 1, z) = \mp 1$. Consequently, as the well-mixed interior region expands, we observe the profile at the walls steepening, developing into separate boundary layers. This is demonstrated in Fig. 9(*a*), in which we plot the streamwise-averaged density $\bar{\rho}$ through the line $z = \pi/2$. At $Pr = 1$, $\bar{\rho}$ has an almost linear profile. By $Pr = 20$, the profile is essentially flat in the interior before becoming highly stratified at the walls. These profiles are reminiscent of turbulent mean temperature profiles of turbulent passively transported scalars simulated by Papavassiliou & Hanratty (1997), of fully stratified turbulence simulations (Zhou *et al.* 2017*a*) and of strongly stratified layers observed in geophysical flows (Turner 1973). See §4 for further discussion.

Simultaneously, the finger-like incursions, or 'density fingers', seen in Fig. 7 start to diminish as the channel becomes increasingly well-mixed. Figure 9(*b*) shows horizontal slices of $\bar{\rho}$ at $y = -0.5$. We see that these structures progressively narrow as Pr increases. Moreover, from $Pr = 5$ to $Pr = 20$ their 'height' ($\max_z \bar{\rho}$) and 'prominence' ($\max_z \bar{\rho} - \min_z \bar{\rho}$) diminishes. These observations are consistent with the emerging homogenisation of the channel interior region through the plane $z = \pi/4$, seen in Fig. 8.

It is the diminishing length scales described above that make obtaining solutions at high Prandtl number numerically expensive, ultimately forcing us to cut short some of the continuation curves in Fig. 2, since states demand increasingly high wall-normal and (to a lesser extent)
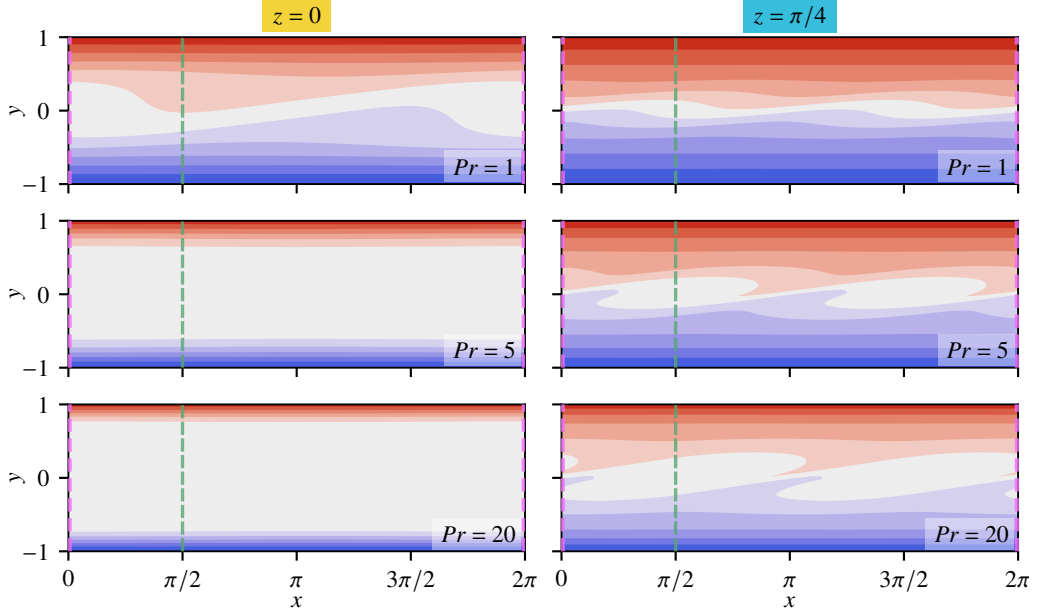
FIGURE 8. Contour slices through xy-planes, of $\rho(x, y, z)$, at $z = 0$ (left column) and $z = \pi/4$ (right column) of the EQ_7 state at at $Pr = 1$, 5 and 20 (top to bottom) and $Ri_b = 0.01$. The solutions match those depicted in Fig. 7, as do the contour intervals. The coloured dashed lines at $x = 0$ and $\pi/2$ mark the locations of the contour slices depicted in Fig. 7.
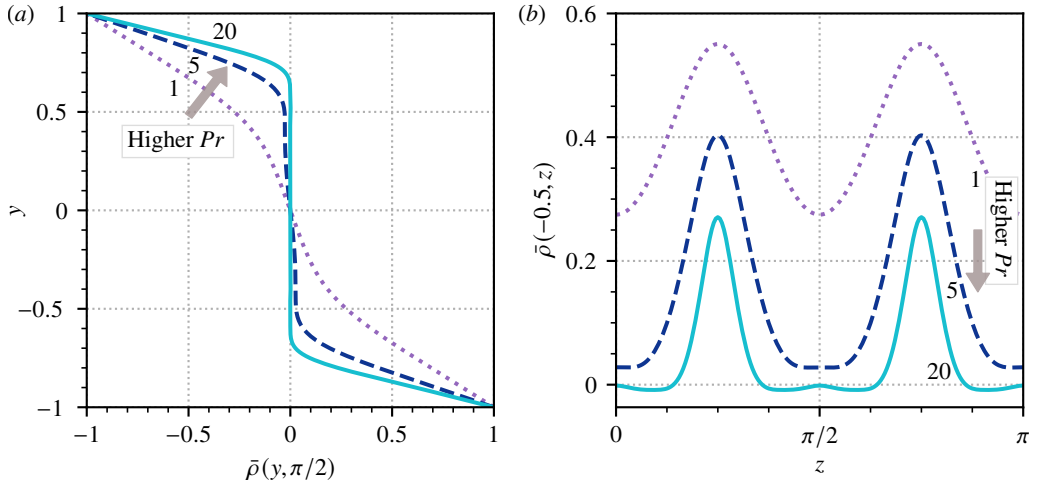

FIGURE 9. Localisation of stratification as Pr increases. The data are from the $Ri_b = 0.01$ solutions depicted in the contour plots of Figs. 7 and 8. The Prandtl numbers are: $Pr = 1$ (purple dotted), $Pr = 5$ (navy dashed), $Pr = 20$ (cyan solid). (*a*) Vertical profiles of $\bar{\rho}(y, z)$ for fixed $z = \pi/2$, showing the development of boundary layers at the walls. (*b*) Horizontal slices of $\bar{\rho}(y, z)$ for fixed $y = -0.5$, showing the shrinking width and magnitude of the regions of extremal density uplifted from the boundaries.

spanwise resolution as Pr increases. Accurately converging states in situations where structures become spatially localised is an important future challenge (see also Olvera & Kerswell 2017). In the following section we obtain higher Prandtl numbers by moving to a regime where we need only solve for the density field (see Appendix A.)
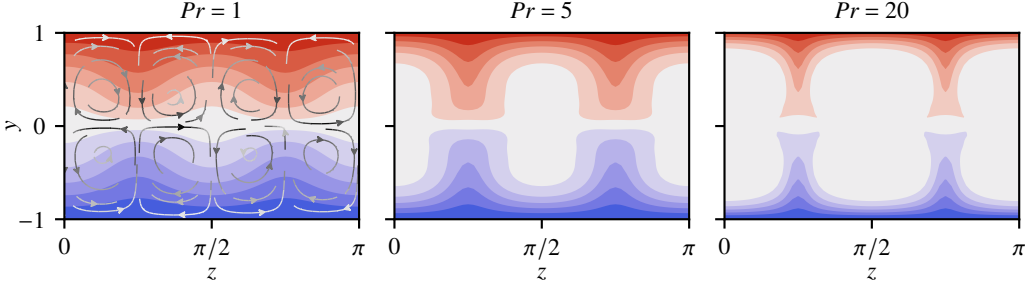
FIGURE 10. Contour plots of $\bar{\rho}_{PS}(y, z)$ for increasing Pr in the channel cross-section. From left to right: $Pr = 1$, $Pr = 5$ and $Pr = 20$ are shown. The contour intervals match those in Fig. 7. Overlaid on the leftmost plot are streamlines of the $(\bar{v}, \bar{w})$-field (which is the same for all three solutions), coloured with a linear gradient from white to black according to the magnitude of $(\bar{v}, \bar{w})$, which lies in the interval $[0, 0.02]$.

3.2.1. *Passive scalar limit ($Ri_b \to 0$)*

The passive scalar limit, $Ri_b \to 0$, offers key insight into these high-Pr solutions, since in this regime the momentum equation [Eq. (2.1a)] decouples from the density field.. We hereafter adopt the notation ρ_{PS} for the density fields in this limit. The uncoupling of momentum from density allows the stratification equation [Eq. (2.1c)] to be studied independently from the velocity field, which is just that of the unstratified equilibrium state. Numerically, this limit can be accessed simply by setting $Ri_b = 0$ in the nondimensionalised system, Eqs. (2.1a)–(2.1c). Figure 10 shows the streamwise-averaged passive scalar density field, $\bar{\rho}_{PS}$, for EQ_7 at three successively increasing Pr. This reveals an underlying structure of stacked rolls and their advective influence on the density field. Much of the character of the density fields described above persists in the $Ri_b = 0$ case. In particular, the spanwise-localised fingers remain, as does the stratified boundary layer, which rapidly diminishes with increasing Pr, leaving a largely homogeneous interior.

The increasing concentration of ρ_{PS} at the boundaries indicates that high-Pr solutions must involve a separation of length scales. Considering a boundary layer of thickness ϵ at the bottom boundary $y = -1$, we define a scaled vertical coordinate $Y := (y + 1)/\epsilon$ and Taylor expand the leading order (VWI) velocity field across the layer

$$u(x, y, z) = -1 + \epsilon u_1(x, z)Y + \dots \tag{3.5a}$$

$$v(x, y, z) = \epsilon^2 Re^{-1} v_2(x, z)Y^2 + \dots \tag{3.5b}$$

$$w(x, y, z) = \epsilon Re^{-1} w_1(x, z)Y + \dots \tag{3.5c}$$

using the boundary conditions ($u + 1 = v = w = 0$ at $Y = 0$) and incompressibility ($\partial v/\partial y = 0$ at $Y = 0$). Since the boundaries are well away from the critical layer at $y = 0$, the flow fields (as $Re \to \infty$) have the form

$$u_1(x, z) = \bar{u}_1(z) + Re^{-7/6} U_1(x, z) + \dots, \tag{3.6a}$$

$$v_2(x, z) = \bar{v}_2(z) + Re^{-1/6} V_2(x, z) + \dots, \tag{3.6b}$$

$$w_1(x, z) = \bar{w}_1(z) + Re^{-1/6} W_1(x, z) + \dots \tag{3.6c}$$

It is straightforward to argue that ρ_{PS} must be streamwise-invariant at leading order (see Appendix B) so that an appropriate expansion for the density field inside the boundary layer is

$$\rho_{PS}(x, Y, z) = \rho_0(Y, z) + \epsilon \rho_1(x, Y, z) + \dots, \tag{3.7}$$

where the functions ρ_0 and ρ_1 are $O(\epsilon^0)$. On substituting Eqs. (3.5a), (3.5b) and (3.5c) into Eq. (2.1c), along with the asymptotic expansion for the density field and dropping all $O(\epsilon^2)$
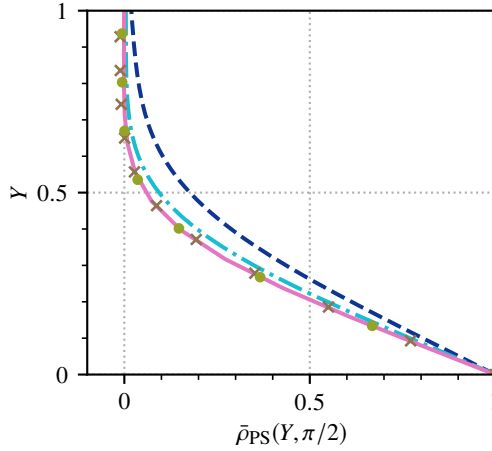
FIGURE 11. Verification of the boundary layer thickness $\epsilon = Pr^{-1/3}$. Streamwise-averaged density profiles through $z = \pi/2$ are shown, plotted near the wall using boundary layer co-ordinates $Y := Pr^{1/3}(y+1)$. The data are from EQ_7 in the passive scalar limit, at $Pr = 5$ (navy dashed), $Pr = 20$ (turquoise dash–dot), $Pr = 100$ (brown crosses), $Pr = 300$ (olive circles) and $Pr = 500$ (pink solid). The three highest Prandtl number profiles collapse almost exactly in the rescaled wall-normal co-ordinates.

terms, we obtain the following leading-order stratification equation:

$$-\epsilon Re \frac{\partial \rho_1}{\partial x} + \epsilon v_2(x,z)Y^2 \frac{\partial \rho_0}{\partial Y} + \epsilon w_1(x,z)Y \frac{\partial \rho_0}{\partial z} = \frac{1}{\epsilon^2 Pr} \frac{\partial^2 \rho_0}{\partial Y^2}. \tag{3.8}$$

Balancing advection with diffusion then requires

$$\epsilon = Pr^{-1/3}, \tag{3.9}$$

which is confirmed in Fig. 11 by plotting $\bar{\rho}_{PS}(Y,z)$ through the line $z = \pi/2$ (other values show similar collapse as long as they are not within the finger-like structures). In these co-ordinates, the density profiles collapse onto each other almost exactly at high Pr ($\gtrsim 100$).

Equation (3.8) splits into a streamwise-independent part which defines ρ_0 and a streamwise-dependent part which defines ρ_1 given ρ_0 as follows:

$$\bar{v}_2(z)Y^2 \frac{\partial \rho_0}{\partial Y} + \bar{w}_1(z)Y \frac{\partial \rho_0}{\partial z} = \frac{\partial^2 \rho_0}{\partial Y^2}, \tag{3.10a}$$

$$Re^{-7/6} V_2(x,z)Y^2 \frac{\partial \rho_0}{\partial Y} + Re^{-7/6} W_1(x,z)Y \frac{\partial \rho_0}{\partial z} = \frac{\partial \rho_1}{\partial x}. \tag{3.10b}$$

Using incompressibility, $\bar{w}_1'(z) = -2\bar{v}_2(z)$, the leading balance, Eq. (3.10a), becomes

$$\frac{\partial^2 \rho_0}{\partial Y^2} + \frac{1}{2}\bar{w}_1'(z)Y^2 \frac{\partial \rho_0}{\partial Y} = \bar{w}_1(z)Y \frac{\partial \rho_0}{\partial z}, \tag{3.11}$$

with the boundary conditions $\rho_0(0,z) = 1$ and $\rho_0(Y,z) \to 0$ as $Y \to \infty$ to match onto a homogenised interior.

At stagnation points z^* where the spanwise velocity is zero, the right hand side of Eq. (3.11) vanishes and it reduces to an ordinary differential equation for ρ_0. A solution of this, which decays as it leaves the boundary layer ($Y \to \infty$), is

$$\rho_0(Y,z^*) = 1 - \frac{(9|\bar{v}_2|)^{1/3}}{\Gamma(1/3)} \int_0^Y \exp\left(\frac{1}{3}\bar{v}_2 s^3\right) ds, \tag{3.12}$$

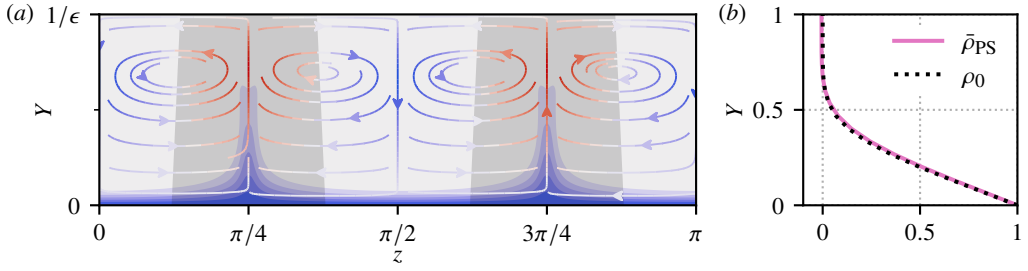and only exists if $\bar{v}_2 < 0$, i.e. if there is inflow towards the $y = -1$ wall. Figure 12(a) shows

FIGURE 12. (*a*) Plot of $\bar{\rho}_{PS}(Y, z)$ in the half-channel $0 \leqslant Y \leqslant 1/\epsilon$, for $Pr = 300$, contoured with intervals matching those in Fig. 7. The streamlines show the streamwise-averaged fluid motion in the (Y, z)-plane and are coloured from blue (inflow toward the wall), to white ($\bar{v} = 0$), to red (outflow from the wall) according to the value of $\bar{v}$. Regions of outflow are shaded grey. (*b*) Asymptotic density profile $\rho_0(Y, z^*)$ [Eq. (3.12)], (black dotted, computed with $\bar{v}_2 = -36.2$ to 3 s.f.), plotted alongside the streamwise-averaged density $\bar{\rho}_{PS}(Y, z^*)$ at $Pr = 300$, for the inflow stagnation point at $z^* = \pi/2$.

a contour plot of $\bar{\rho}_{PS}(Y, z)$ at high Prandtl number, $Pr = 300$. The density boundary layer is approximately uniform in the spanwise direction where there is inflow into the boundary layer and the asymptotic solution [Eq. (3.12)] matches the numerical solution at the inflow stagnation points: see Fig. 12(*b*).

Significantly, there is no equivalent solution of the form in Eq. (3.12), for an 'outflow' stagnation point. This is because these points, $z = \pi/4$ and $3\pi/4$, are the focus of boundary layer eruptions [see Fig. 12(*a*)], where the layer scaling breaks down. These eruptions are the $Ri_b \rightarrow 0$ manifestation of the fingers seen in Fig. 9 for $Ri_b = 0.01$. The situation is clearest at high Re where the flow and density field are dominantly streamwise-independent. Defining a length scale δ for the spanwise width of the fingers, the velocity fields may be Taylor expanded about the outflow stagnation points $(y, z) = (-1, z^*)$ as follows: $\bar{v}(Y, Z) = \epsilon^2 Re^{-1} A Y^2 + O(\epsilon^2 \delta, \epsilon^3)$, and (using incompressibility) $\bar{w}(Y, Z) = -2\epsilon \delta Re^{-1} A Y Z + O(\epsilon^2 \delta, \epsilon \delta^2)$, where $Z := (z - z^*)/\delta$ and A is an $O(Pr^0)$ constant. Then, instead of Eq. (3.8), we have

$$\epsilon A Y^2 \frac{\partial \rho_0}{\partial Y} - 2\epsilon A Y Z \frac{\partial \rho_0}{\partial Z} = \frac{1}{Pr}\left(\frac{1}{\epsilon^2}\frac{\partial^2 \rho_0}{\partial Y^2} + \frac{1}{\delta^2}\frac{\partial^2 \rho_0}{\partial Z^2}\right). \tag{3.13}$$

As the flow in the boundary layer approaches an outflow stagnation point, it enters a corner region where the cross-stream diffusion becomes subdominant. (See Childress (1979) and Childress & Gilbert (1995), pages 135–136, for a discussion of this for an equivalent magnetic field problem, although note that there the velocity boundary conditions used there are stress-free rather than non-slip conditions here.) Therefore, the density field is simply advected by the flow and the leading balance is

$$\epsilon A Y^2 \frac{\partial \rho_0}{\partial Y} - 2\epsilon A Y Z \frac{\partial \rho_0}{\partial Z} = 0. \tag{3.14}$$

This has a solution of the form $\rho_0 = \rho_0(\psi)$ where $\psi := A(\epsilon Y)^2 \delta Z$ is a streamfunction.

Consider a streamline starting in the boundary layer where $(\epsilon, \delta) = (Pr^{-1/3}, 1)$. Then $\psi = O(Pr^{-2/3})$, requiring ϵ and δ to satisfy the condition

$$\epsilon^2 \delta = Pr^{-2/3} \tag{3.15}$$

as the streamline negotiates the corner. In the corner itself, $\epsilon = \delta$ (this is the scaling of the closest point of approach of the streamline to the stagnation point), so the corner is defined by the scalings

$$\epsilon = \delta = Pr^{-2/9}.$$

As the streamline leaves the corner region (with δ decreasing) to enter the outer finger region,
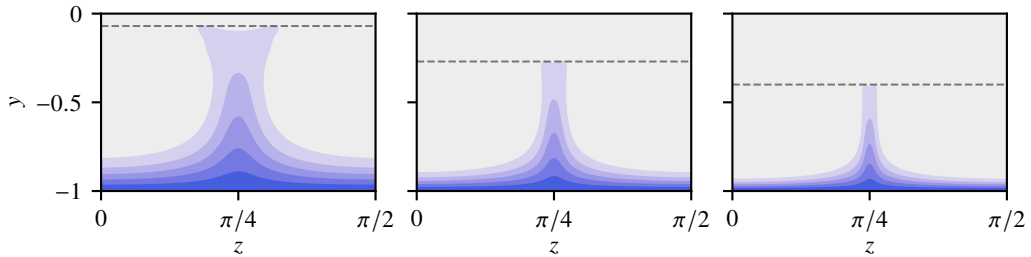
FIGURE 13. Density fingers diminishing with increasing Pr in the passive scalar limit. Plotted are contours of $\bar{\rho}_{PS}(y,z)$ at (from left to right) $Pr = 20$, 100 and 400. The contour intervals match those in Fig. 7. We only plot the bottom left quadrant of the full channel – the other parts are dictated by the solution symmetries. The dashed grey lines indicate the approximate height of the finger structures, at $y = -0.07$, -0.27 and -0.4 respectively.

spanwise diffusion grows to balance advection, so that

$$\epsilon AY^2 \frac{\partial \rho_0}{\partial Y} - 2\epsilon AYZ \frac{\partial \rho_0}{\partial Z} = \frac{1}{Pr\delta^2} \frac{\partial^2 \rho_0}{\partial Z^2}, \tag{3.16}$$

which requires

$$\epsilon \delta^2 = Pr^{-1}. \tag{3.17}$$

Combining the conditions (3.15) and (3.17) leads to outer finger scalings of

$$\epsilon = Pr^{-1/9}, \quad \delta = Pr^{-4/9}. \tag{3.18}$$

Significantly, this predicts that the extent of the fingers' intrusion into the interior will ultimately vanish (albeit slowly) as $Pr \to \infty$ in this $Ri_b \to 0$ limit, consistent with the contour plots in Fig. 13. Unfortunately, the Prandtl numbers reached here are not large enough to confirm this small exponent. What *is* possible is to examine the lower finger profile or corner region. Figure 14(a) shows that streamwise-averaged density profiles through the centreline of the fingers can be collapsed by a rescaled wall-normal co-ordinate $Y_f := (y + 1)Pr^{2/9}$, i.e. the lower parts (corner regions) of the fingers scale like $Pr^{-2/9}$ in y. Figure 14(b) plots spanwise density profiles of $\bar{\rho}_{PS}$, across the finger at $z = \pi/4$, at three fixed $Y_f = 0.25$, 0.5 and 1. On rescaling the spanwise coordinate by $Pr^{2/9}$, the subsequent profiles, ranging from $Pr = 100$ to 400, collapse well.

The important findings from this passive scalar limit are: (a) a rationale for an $O(Pr^{-1/3})$ density boundary layer being formed; (b) the existence of boundary layer eruptions, producing *fingers*, centred at outflow stagnation points in the boundary layer; and (c) the fact that these eruptions are actually secondary (they diminish with increasing Pr) to the primary result that the density gets more and more confined to boundary layers, leaving an homogenised interior as $Pr \to \infty$. We now examine whether this picture holds more generally for $Ri_b > 0$ equilibria.

3.2.2. $Ri_b > 0$

We now look at how the lower branch solutions behave as Ri_b is increased from zero. In Fig. 15(a), we replot the lower branch data from Fig. 2(b) on semi-log axes, for low Ri_b and $Pr \geqslant 40$ (where the boundary layer and finger structures are well developed). As in both the low Pr and $Pr = O(1)$ (Deguchi 2017; Olvera & Kerswell 2017) cases, there is necessarily a passive scalar regime where the momentum and stratification equations [Eqs. (2.1a) and (2.1c)] remain effectively uncoupled. This is the approximately horizontal part of the solution branch, from $Ri_b = 0$ to $Ri_b \approx 10^{-3}$. The fact that the upper limit of this regime does not display any dependence on Pr contrasts with the scaling of $Ri_b = O(Pr^{-1}Re^{-2})$ for $Pr \lesssim O(1)$ (Deguchi 2017; Olvera & Kerswell 2017, and §3.1) in which Ri_b scales inversely with Pr. The difference here when $Pr \gg 1$ is that the density perturbation $\hat{\rho}$ has to be $O(1)$ to homogenise the interior. The buoyancy force
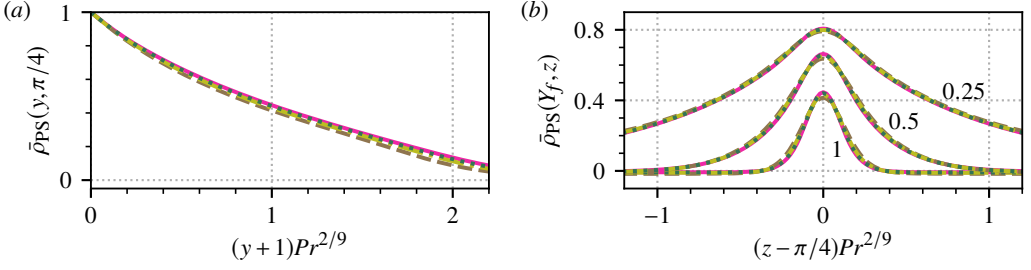
FIGURE 14. Scaling of density fingers at high Pr. Both parts plot slices through the same set of solutions in the passive scalar limit, with Prandtl numbers $Pr = 100$ (brown dashed), $Pr = 200$ (olive dash–dot), $Pr = 300$ (dark green dotted) and $Pr = 400$ (magenta solid). (*a*) Streamwise-averaged density $\bar{\rho}_{PS}$ through the finger-like structure at $z = \pi/4$, as a function of the rescaled wall-normal co-ordinate $Y_f := (y+1)Pr^{2/9}$. (*b*) Streamwise-averaged density profiles in the spanwise co-ordinate, rescaled in the vicinity of the finger structure at $z = \pi/4$ by $Pr^{2/9}$. For each Prandtl number, three slices are plotted at fixed $Y_f = 0.25, 0.5$ and 1 as indicated.
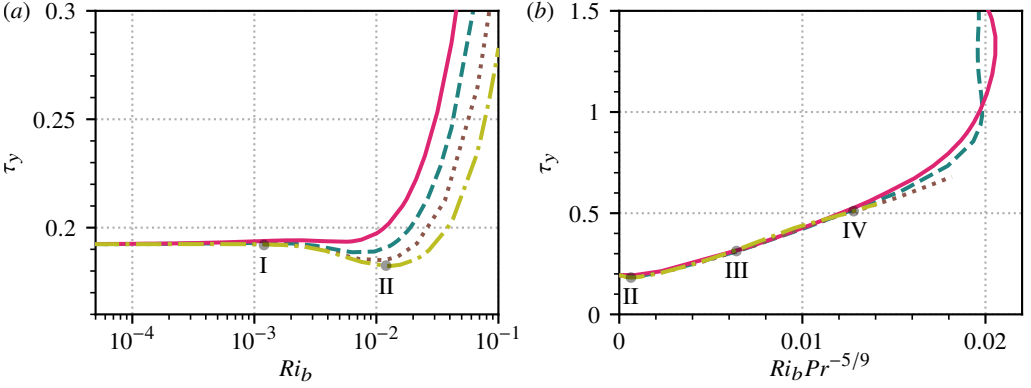

FIGURE 15. Sections of the high-Pr solution curves from Fig. 2(*b*) along the lower branch. Shown are $Pr = 40$ (magenta solid), 70 (teal dashed), 120 (brown dotted), 200 (olive dash–dot). (*a*) Low Ri_b portion with logarithmic horizontal axis. (*b*) The lower branch plotted with the horizontal axis rescaled by $Pr^{-5/9}$. In both parts, the numerals I–IV indicate the locations of solutions plotted below in Figs. 16–18.

is then $O(Ri_b)$ and the streamwise rolls first feel its influence when $Ri_b = O(Re^{-2})$. It is worth noting that this argument relies on the fact that the interior is only partly homogenised, otherwise $\hat{\rho} = y$ would precisely cancel out the linear base profile and then the buoyancy force can be exactly balanced by the pressure.

Just beyond $Ri_b = 10^{-3}$ in Fig. 15(*a*), the lower branch solutions all experience a small drop in stress at the walls. The reason for this is encapsulated in Fig. 16(*a*), where streamwise-averaged density slices through the yz-plane are plotted for the $Pr = 200$ density field at $Ri_b = 1.2 \times 10^{-3}$ (point I, Fig. 15) and 1.2×10^{-2} (point II, Fig. 15), with streamwise velocity contours overlaid. Between these two bulk Richardson numbers, the four streaks centred at $z = \pi/4$ and $3\pi/4$ noticeably weaken and recede from the walls. Increasing Ri_b penalises the upward motion of dense fluid and likewise the downward motion of less-dense fluid. Consequently, we observe in Fig. 16(*b*), that the magnitude of the $\bar{v}$ field drops significantly for $0.3 \lesssim |y| \lesssim 1$, in the vicinity of the density fingers, leading to the weakening of the streaks there. This is highlighted further in Fig. 16(*c*), where we plot streamwise-averaged slices of $\hat{u}$ through $z = \pi/4$ and see that it drops along the approximate length of the fingers. The density fingers also retreat as Ri_b increases, since they are no longer vertically advected as strongly. The streaks centred at $z = 0 \equiv \pi$ and $\pi/2$ are largely unaffected, since they only experience significant buoyancy forces in the thin
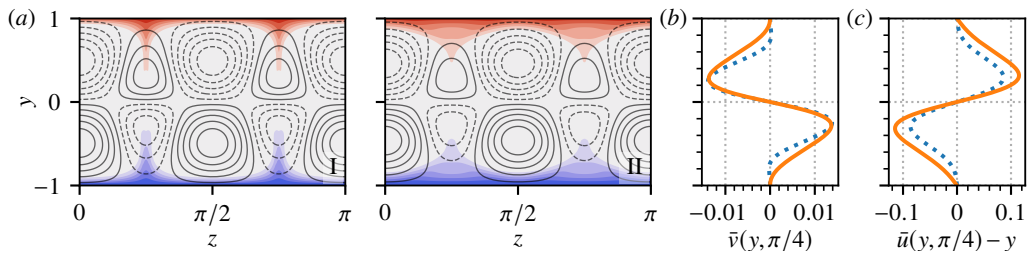
Effect of Prandtl number on stably stratified exact coherent structures   19

FIGURE 16. Plots demonstrating the stress drop in the high-Pr lower branch states. (*a*) Comparison of EQ_7 at $Pr = 200$ and $Ri_b = 1.2 \times 10^{-3}$ (left) and 1.2×10^{-2} (right), located at points I and II on Fig. 15(*a*) respectively. The plots show $\bar{\rho}$ contours in the yz-planes, plotted from red ($\bar{\rho} < 0$) to blue ($\bar{\rho} > 0$), using intervals matching those in Fig. 7. Overlaid in black lines are 10 isolines of the streamwise-averaged $\hat{u}$ field, separated by equally spaced intervals between ± 0.2. Dashed lines represent $\bar{u} - y < 0$, solid lines $\bar{u} - y > 0$. (*b*) Profiles of $\bar{v}$ for the solutions depicted in part (*a*), through $z = \pi/4$. (*c*) Corresponding profiles of $\bar{u} - y$, through $z = \pi/4$. In parts (*b*) and (*c*), solid orange lines are the $Ri_b = 1.2 \times 10^{-3}$ state (I) and dashed blue lines are the $Ri_b = 1.2 \times 10^{-2}$ state (II).

boundary layer. Therefore, there is a small reduction in mean wall stress in this regime, caused by the streamwise flow receding from the wall in the finger regions.

Following the mean stress drop, there is a marked and sustained rise in τ_y as Ri_b increases further and states enter a new regime, which covers most of the lower branch. Working on the basis that it is the stratification invading the interior which exerts the leading influence on the ECS, a simple estimate for how Ri_b varies with Pr can be deduced as follows. Assuming the passive scalar finger scalings, the fingers represent an $O(1)$ stratification perturbation to the interior in a volume of size $O(1) \times O(Pr^{-1/9}) \times O(Pr^{-4/9})$. This is equivalent to an $O(Pr^{-5/9})$ stratification over the entire $O(1)$ volume which could be expected to influence the wall-normal momentum equation when $Re^{-2} \sim Ri_b Pr^{-5/9}$ (balancing viscous diffusion with the buoyancy term) or $Ri_b = O(Pr^{5/9})$. While the finger scales are by no means guaranteed to persist beyond the weakly stratified regime, Fig. 15(*b*) demonstrates a remarkably good collapse of the data.

Figure 17 shows yz-contours of the streamwise-averaged streak field $\bar{u} - y$, overlain on $\bar{\rho}$, for states at three stages along the lower branch, namely the (rescaled) locations labelled on Fig. 15(*b*): $Ri_b Pr^{-5/9} = 6.4 \times 10^{-4}$ (point II, at the stress drop), 6.4×10^{-3} (point III) and 1.28×10^{-2} (point IV). The similarity between the $Pr = 70$ and the $Pr = 200$ fields is immediately striking, with the principal difference only being that the $Pr = 200$ density field is slightly more homogenised in the interior. In both cases, we see the streak field developing in a similar way to the low Pr states (see Fig. 4); the wall outflow streaks at $z = \pi/4$ and $3\pi/4$ recede into the interior, become dominated by the inflow streaks at $z = 0 \equiv \pi$ and $\pi/2$ (point III), and the streamwise velocity perturbation separates into negative and positive halves (point IV).

The $\bar{v}$ fields corresponding to the Fig. 17 lower branch states are plotted in Fig. 18, again with $\bar{\rho}$ underlaid. At the stress drop (II), the $\bar{v}$ field covers the full interior, though it is somewhat inhibited in the finger regions. By point III (one third along the lower branch) it has pulled away completely from the highly stratified regions at the walls and remains that way as Ri_b increases to point IV (two thirds along the lower branch). Meanwhile, the density fingers have smeared out and the stratified layer has thickened, due to readjustment of the advective-diffusive balances there. It is worth noting that the magnitude of $\bar{v}$ in the interior has increased substantially. This leads to the growth of the streak fields and the corresponding mean stress increases along the lower branch (see Figs. 15(*b*) and 17). However, the main message is that faced with increasing stratification at the walls, the $\bar{v}$ field isolates itself, pulling in towards the homogenised interior, where $\bar{\rho} \approx 0$. This appears to be a key mechanism via which the ECS extends the range of Ri_b at which it can persist before being disrupted. As Pr increases for any fixed Ri_b, the stratified layer
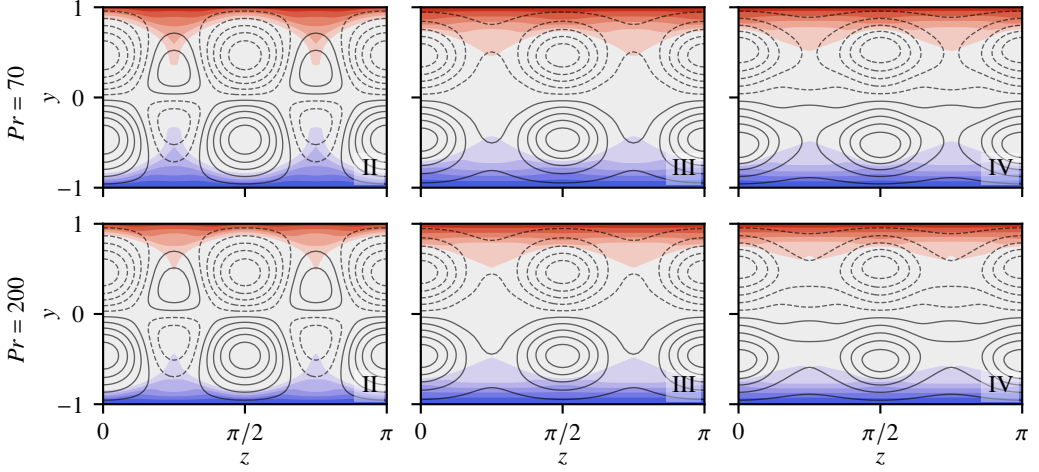
FIGURE 17. Streamwise-averaged contour plots of EQ_7 at high Pr along the ($Pr^{-5/9}$-rescaled) lower branch, at the points II–IV, as indicated in Fig 15(b); $Ri_b Pr^{-5/9} = 6.4 \times 10^{-4}$ (II), 6.4×10^{-3} (III) and 1.28×10^{-2} (IV), with $Pr = 70$ (top row) and 200 (bottom row). Contours of $\bar\rho(y,z)$ are shown, plotted from red ($\bar\rho > 0$) to blue ($\bar\rho < 0$); intervals match those in Fig. 7. Overlaid in black are 10 evenly spaced isolines of the streamwise average of $\hat u$, between ± 0.2 (II), ± 0.29 (III) and ± 0.37 (IV). Dashed lines are negative contours and solid lines are positive. For reference, the bulk Richardson numbers for the $Pr = 70$ data are 6.8×10^{-3} (II), 6.8×10^{-2} (III), and 0.14 (IV). For the $Pr = 200$ data, $Ri_b = 1.2 \times 10^{-2}$ (II), 0.12 (III), and 0.24 (IV).
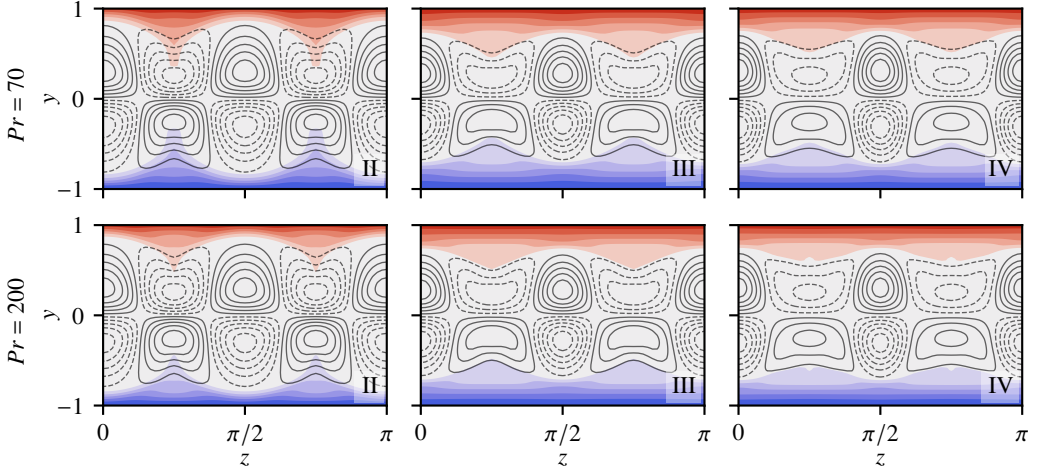

FIGURE 18. Evolution of the $\bar v$ field for increasing Ri_b along the high-Pr lower branches, $Pr = 70$ (top row) and 200 (bottom row). Each pane features 10 equally spaced isolines of $\bar v$ corresponding to the states shown in Fig. 17, located at points II–IV along the solution branches in Fig. 15(b). The isolines lie between ± 0.015 (II), ± 0.031 (III) and ± 0.05 (IV), with solid lines indicating $\bar v > 0$ and dashed lines $\bar v < 0$. Underneath, the $\bar\rho(y,z)$ contours (shown in Fig. 17) are replotted for reference. The bulk Richardson numbers for the $Pr = 70$ data are 6.8×10^{-3} (II), 6.8×10^{-2} (III), 0.14 (IV) and for the $Pr = 200$ data: $Ri_b = 1.2 \times 10^{-2}$ (II), 0.12 (III) and 0.24 (IV).

recedes further into the walls and the effect of Ri_b on the structure is less severe. Indeed, our data and associated scaling argument hints that the maximum bulk Richardson number attained by states is $Ri_b^m = O(Pr^{5/9})$, though it is currently challenging to verify this concretely, given the numerical difficulties inherent in resolving high-Pr states and their shrinking length scales.

3.2.3. *Other solutions*

While Olvera & Kerswell (2017) isolated EQ_7 & EQ_8 by tracking the edge manifold, many other equilibria exist in plane Couette flow that are dynamically important in the unstratified setting. Since these states, which typically enjoy fewer symmetries than the EQ_7 / EQ_8 branch, are nevertheless based upon the same SSP/VWI tripartite structure of rolls, streaks and waves, the expectation is that our findings of density homogenisation in the interior with stably stratified boundary layers forming as a consequence at high Prandtl number are generic. To confirm this, we continued solutions EQ_1–EQ_{11} from Gibson *et al.* (2009) to increasing Pr in the passive scalar limit ($Ri_b \to 0$) and observed how they change as density transport becomes increasingly convectively dominated.

Figure 19 shows contours of $\bar{\rho}(y, z)$ for a subset of our converged solutions at $Pr = 1$ (lefthand column), 10 (middle column) and 70 (righthand column), with overlaid streamlines on the lefthand column depicting the different roll structures. Just as for EQ_7 in §3.2.1, each of these new solutions develops a homogenised interior with a corresponding highly stratified boundary layer at the walls. Importantly, each solution features characteristic density fingers, advected into the interior by the rolls, which shrink as Pr increases to leave an increasingly homogenised interior. The solutions EQ_4, EQ_6, EQ_9 and EQ_{11} (not shown) behave similarly.

4. Discussion

In this study, we have computed exact coherent structures (ECS) in stratified plane Couette flow across a wide range of Prandtl numbers at a fixed Reynolds number $Re = 400$. In the two asymptotic limits $Pr \ll 1$ and $Pr \gg 1$, states persist to arbitrarily high bulk Richardson numbers, in spite of the stabilising influence of stratification. However, the underlying mechanisms which allow this in each case are quite different.

In the $Pr \to 0$ limit, density transport is diffusion dominated with perturbations from the constant base density gradient being only $O(Pr)$. To leading order, the bulk Richardson number Ri_b only affects the ECS in the combination $Ri_b Pr$ with stratification having no noticeable effect on the flow until $Ri_b = O(Pr^{-1}Re^{-2})$. Beyond this regime, states continue to follow an $O(Pr)$ asymptotic solution curve, reaching a maximum value of $Ri_b^m \approx 0.01/Pr$ at $Re = 400$, for the ECS studied in detail here (EQ_7).

In the $Pr \to \infty$ limit, density transport is advection dominated for any $Ri_b > 0$, with the interior becoming homogenised as the stratification is confined to boundary layers at the walls (their thickness being $O(Pr^{-1/3})$ in the $Ri_b \to 0$ limit). The flow and the density stratification are then separated into different parts of the domain with the stratification only starting to influence the velocity field when $Ri_b = O(Re^{-2})$ independently of Pr, which differs from the $Pr \lesssim O(1)$ scaling of $O(Pr^{-1}Re^{-2})$ (Deguchi 2017; Olvera & Kerswell 2017). The maximum stratification which can be tolerated by the ECS looks to be $Ri_b^m \sim O(Pr^{5/9})$ at fixed Re. Numerically, the situation at large but finite Pr and small Ri_b is complicated by eruptions in the density boundary layers at regions of outflow. These eruptions give rise to *fingers*, which ultimately vanish to leave a homogenised interior in the limit $Pr \to \infty$. This behaviour is qualitatively captured in the passive scalar limit ($Ri_b \to 0$) where these fingers have spanwise width $O(Pr^{-2/9})$ near the wall, contracting to $O(Pr^{-4/9})$ further away and wall-normal length $O(Pr^{-1/9})$.

As discussed in the introduction, a dynamical systems perspective of stratified turbulence imagines a 'turbulent' trajectory guided through a complicated phase space by a hierarchy of simple invariant solutions (ECS) and their entangled stable and unstable manifolds. Therefore, it is reasonable to expect that understanding the structure of ECS as a function of the parameters Re, Pr and Ri_b may help explain what is seen (maybe fleetingly) in stratified turbulence. Here, we have found simple (laminar) realisations of boundary layers and homogenised regions seen
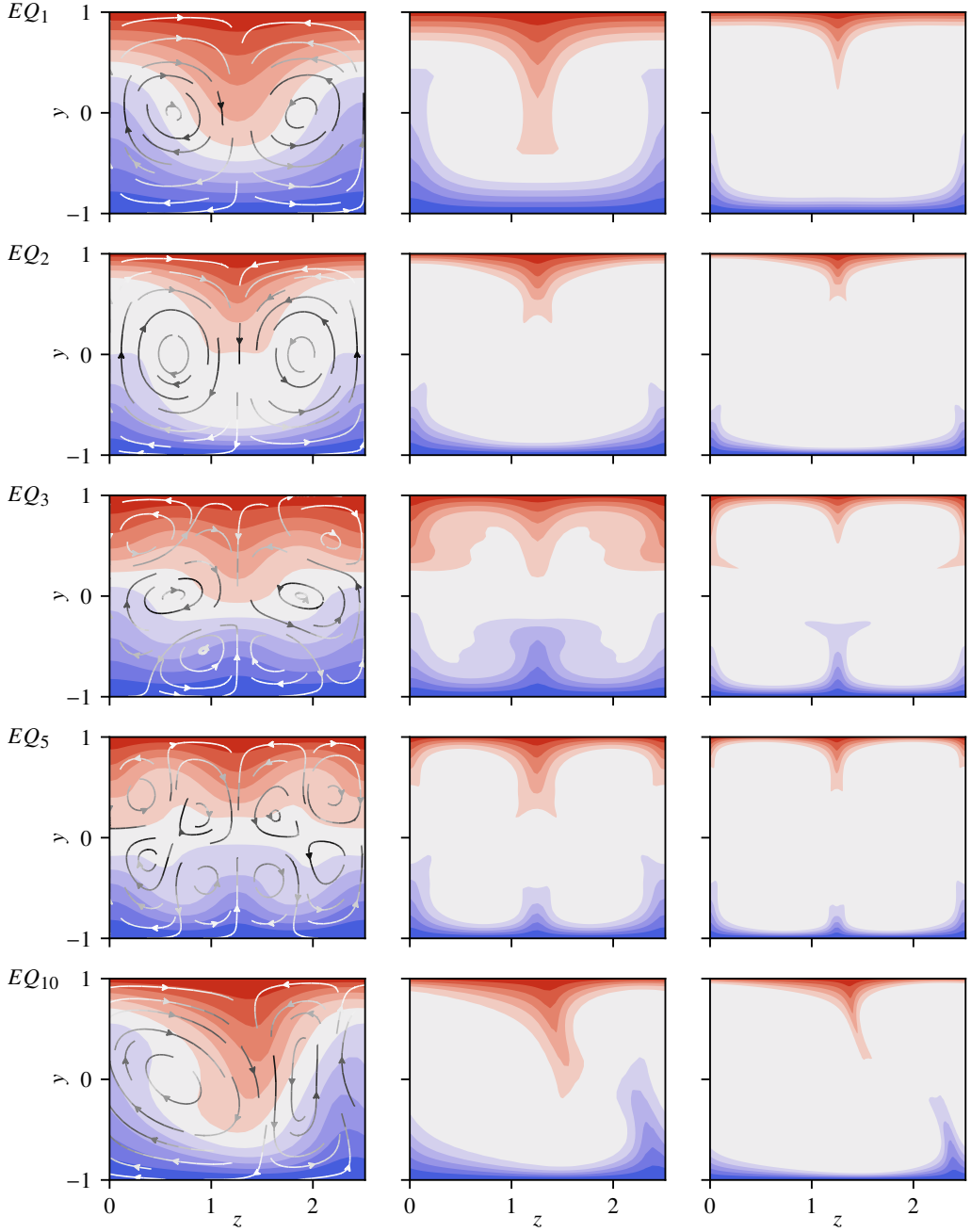
FIGURE 19. Streamwise-averaged density fields $\bar{\rho}(y, z)$ for various equilibria in the passive scalar limit. The columns increase in Prandtl number from left to right: $Pr = 1$, 10 and 70. The contour intervals match those in Fig. 7. Streamlines of $(\bar{v}, \bar{w})$ are shown on the leftmost plots, coloured with a linear gradient from white to black, according to $|(\bar{v}, \bar{w})|$, which has a maximum value of (to 2 significant figures): 0.018 (EQ_1), 0.098 (EQ_2), 0.033 (EQ_3), 0.053 (EQ_5) and 0.061 (EQ_{10}).

in turbulence with clear scalings emerging, at least for small Ri_b. For example, the $O(Pr^{-1/3})$ boundary layers found here resonate with empirical observations (Kader 1981; Schlichting & Gersten 2016) and recent numerical work (Zhou *et al.* 2017*a*) concerning the thickness of the conductive sublayer. Further work is obviously needed to push these to higher Ri_b and Re, but at least this is a start.

Perhaps most noteworthy is the homogenisation seen at high Pr, where the shear-driven flow simply clears the stratification out of its way. This limit is costly to simulate at high Re since the Péclet number ($Pe := RePr$) is even larger and hence is little explored. However, hopefully our findings here will help encourage more effort to reach this environmentally-relevant limit, since these results clearly highlight the difference between $Pr \sim 1$ and Pr being large, where a value of 70 (let alone 700 for salt in water) is significant enough to see the difference.

While our results concentrated principally on the highly-symmetric EQ_7 / EQ_8 branch, the high-Pr homogenisation of the stratified analogues for the remaining Gibson *et al.* (2009) equilibria demonstrated in §3.2.3 is an indication that this phenomenon is generic. To establish more fully the relevance of these solutions to observations of real stratified flows, it would be desirable to check whether solutions outside the constraints of our small periodic computational domains behave similarly, especially to see if states with no discrete symmetries can be identified. Moreover, there is the question of whether travelling waves and periodic orbits adapt to increasing Pr and Ri_b in the same way. However, the extremely high resolutions needed to obtain these solutions pushes these computations beyond our reach for now.

Looking ahead, the existence of highly stratified boundary layers found here in the large Pr limit begs the question whether stably-stratified *interior* density interfaces could exist for these unstable steady flows. One exploratory computation, taking the EQ_7 solution in the passive scalar limit and increasing Re from 400 to 10^5 indicates 'yes'. Fig. 20(*a*) plots contours of the resulting streamwise-averaged density fields and, from $Pr = 5$ to 70, we see the usual finger structures and boundary layers developing. In this case, however, the top and bottom halves of the channel interior have separated into distinct patches of roughly constant density. In this high-Re regime, the ECS converges to a VWI state, becoming streamwise-invariant to leading order (see §2.2). The symmetries of EQ_7 dictate that $v(x, 0, z) \to 0$ as $Re \to \infty$ (since the flow becomes increasingly streamwise independent and $v(x, 0, z) = -v(-x, 0, z)$). Therefore, while density in the top and bottom half-channels can become well-mixed as Pr increases, there is little exchange between the two. (Note that states such as EQ_1, whose rolls span the full height of the channel, do not enjoy this property).

Fig. 20(*b*) plots the spanwise average of $\bar{\rho}_{PS}(y, z)$ against y for EQ_7 and reveals a highly stratified region at the midplane. In this passive scalar limit where the velocity field is independent of Pr, an advective-diffusive balance sets the thickness of this interface at $O(Pr^{-1/2})$ which is borne out by the limited data here, plotted in Fig. 21(*a*) up to $Pr = 300$. The scaling of the density change across the layer is less clear, though $O(Pr^{-3/4})$ seems to capture its dependence for $Pr \gtrsim 100$ and taken together, these two scales succeed in collapsing the density profiles at the interface in Fig. 21(*b*). Whilst this ultimately implies that the interface vanishes in the $Pr \to \infty$ limit, it is nevertheless finite in the $Pr = O(10^2)$ range most relevant to geophysical phenomena. Clearly more computations need to be done to explore this phenomenon.
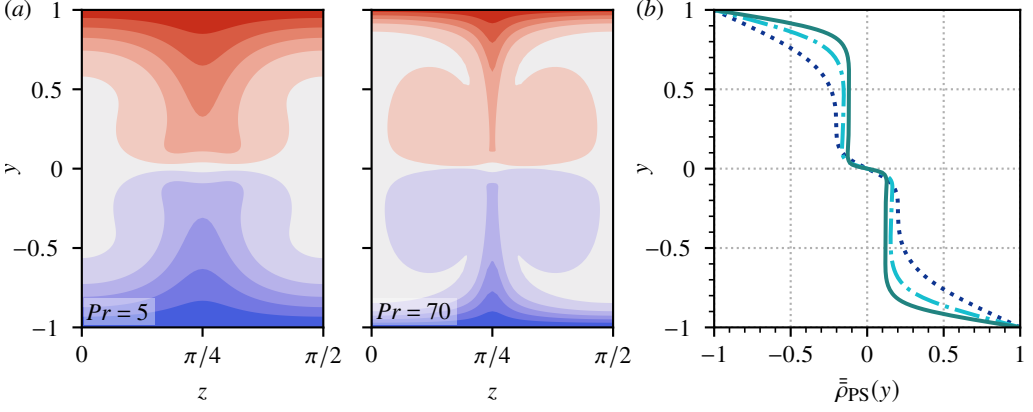
FIGURE 20. Emergence of internal density interfaces as Pr increases at $Re = 10^5$. (*a*) Streamwise-normal contour plots of $\bar{\rho}_{PS}(y, z)$, for $Pr = 5$ (left) and $Pr = 70$ (right). Half the channel ($0 \leqslant z \leqslant \pi/2$) is shown (the rest being dictated by symmetry). (*b*) Spanwise- and streamwise-averaged density profiles $\bar{\bar{\rho}}_{PS} := \frac{1}{L_z} \int_0^{L_z} \bar{\rho}_{PS}(y, z)\,\mathrm{d}z$, for $Pr = 5$ (blue dotted), 20 (turquoise dash-dot) and 70 (teal solid).
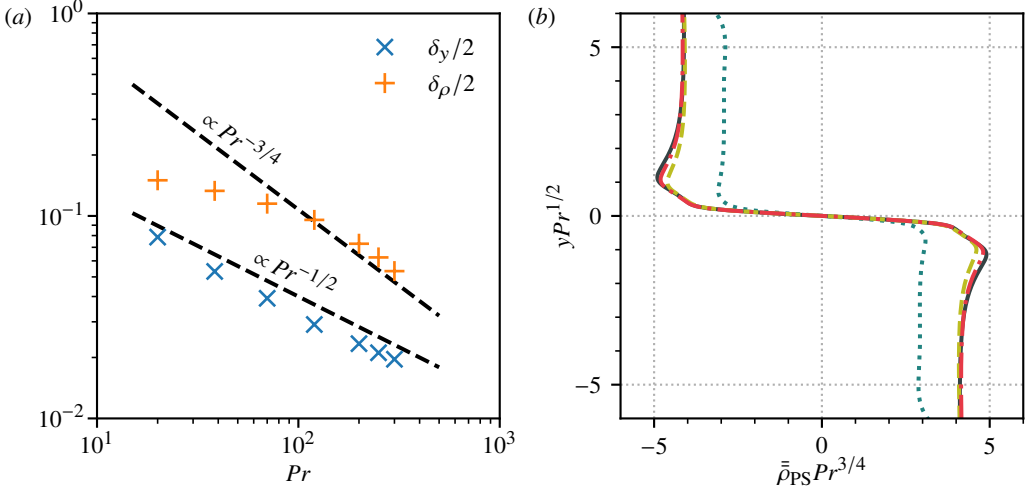

FIGURE 21. Empirical scalings of the high-Re ($= 10^5$), high-Pr internal layers plotted in Fig. 20. (*a*) Log-log plot showing half the interface thickness δ_y (blue $\times$) and half the density change δ_ρ (orange $+$) between the two well-mixed regions, as a function of Pr, ranging from 20 to 300. The two black dashed lines are $0.4Pr^{-1/2}$ and $3.4Pr^{-3/4}$. Across all data points, the interface is contained within the region $\mathcal{I} := (-0.2, 0.2)$ and ρ_{PS} reaches an approximately constant value near the edges of this region. Therefore, the half-thickness $\delta_y/2$ was estimated by $\arg\max_{y \in \mathcal{I}} \bar{\rho}_{PS}(y, 3\pi/8)$ and $\delta_\rho/2$ was estimated using $\bar{\rho}_{PS}(-0.2, 3\pi/8)$. (*b*) Streamwise- and spanwise-averaged density profiles $\bar{\bar{\rho}}_{PS}(y)$, rescaled as indicated, by the observed Pr-dependences in part (*a*). The Prandtl numbers are $Pr = 70$ (teal dotted), 200 (olive dashed), 250 (red dash-dot) and 300 (dark grey solid).

Appendix A. Numerical code details

The flow fields in our direct steady Boussinesq solver are represented by the real part of the truncated pseudo-spectral expansion

$$\sum_{m=-M}^{M} \sum_{n=1}^{N} \sum_{l=-L}^{L} \xi_{n,l,m} F_n(y) e^{i(m\alpha x + l\beta z)} \tag{A 1}$$

for $(x, y, z) \in [0, L_x] \times [-1, 1] \times [0, L_z]$, where $\alpha = 2\pi/L_x$ and $\beta = \pi/L_z$. The $\xi_{n,l,m}$ are unknown complex coefficients and $F_n := F_n^{(r)} + iF_n^{(i)}$ are basis functions in the wall-normal co-ordinate chosen to satisfy the boundary conditions. For $\xi \in \{\hat{u}, \hat{v}, \hat{w}, \hat{\rho}\}$, we have $\xi(\pm 1) = 0$ and use

$$F_n^{(r)} = T_{2n+1} - T_{2n-1}, F_n^{(i)} = T_{2n} - T_{2n-2}, \tag{A 2}$$

where T_n denotes the n-th Chebyshev polynomial; for the pressure field we use

$$F_n^{(r)} = T_{2n-2}, F_n^{(i)} = T_{2n-1}. \tag{A 3}$$

We save memory and computation time by omitting coefficients that are fixed by the symmetries defined in Eqs. (2.6a)–(2.6c). In particular, $\mathcal{S}$ implies that $\xi_{n,l,m} = 0$ if $m + l$ is odd; $\mathcal{Z}$ implies that $\xi_{n,l,m} = \xi_{n,-l,m}$ for $\xi \in \{u, v, p, \rho\}$ and $\xi_{n,l,m} = -\xi_{n,-l,m}$ for $\xi = w$; Ω, together with our basis choices in Eqs. (A 2) and (A 3) leads to $\xi_{n,l,m} = \xi_{n,l,-m}^*$ for $\xi \in \{u, v, p, \rho\}$ and $\xi_{n,l,m} = -\xi_{n,l,-m}^*$ for $\xi = w$, where the asterisk denotes complex conjugation. These relations reduce the number of Fourier modes required from $(2M + 1)(2L + 1) \approx 4ML$ to $\left\lfloor \frac{1}{2}((M+1)(L+1)+1) \right\rfloor \approx ML/2$.

Equilibria are converged by inverting the steady form of Eqs. (2.1a)–(2.1c) for each Fourier mode at the Chebyshev collocation points y_j, defined by

$$-1 < y_j := \cos\left[\frac{\pi(2(j+N)-1)}{4N}\right] < 0, \quad j = 1, \ldots, N. \tag{A 4}$$

Note that the remaining half-channel, $0 \leqslant y \leqslant 1$, need not be discretised, since it is given by Ω.

Solution branches were numerically refined until increasing M, N or L no longer noticeably affected τ_y. Individual states plotted for analysis were typically refined further to ensure that the density field was well-resolved. Typical resolutions were $(M, N, L) = (12, 40, 12)$ in the low-Pr case (see §3.1) and up to a maximum of $(12, 90, 38)$ or $(10, 120, 30)$ for high-Pr states analysed in §3.2. In the passive scalar limit $Ri_b \to 0$, the velocity and pressure fields are independent of density. Consequently, we need only solve Eq. (2.1c) subject to fixed u, v and w fields, achieving higher resolution in ρ as a result. This method was to verify the structure scalings derived in §3.2.1 and to compute the high-Re states discussed in §4, reaching resolutions for the density field of up to $(18, 140, 60)$ and $(4, 650, 68)$ respectively. In all cases the system possessed roughly 200 000 degrees of freedom at maximum resolutions, requiring ≈ 400Gb of computer memory to directly invert the linear operator. Each Newton step at the highest resolutions needed roughly 2 hours of wall-clock time on a single compute node with 28 Intel Xeon E5-2680 2.4GHz cores, making continuation at these resolutions expensive. Tracing out the $Pr = 70$ branch, for example, required about 1 month of wall-clock time.

Details of the Channelflow code used to compute states in §3.2.3 may be found elsewhere (Gibson *et al.* 2008, 2019). This base code was modified to include Eq. (2.1c) in the time stepping routines. The maximum resolution employed was to converge EQ_3 at $Pr = 70$ and used a discretised box with $(N_x, N_y, N_z) = (120, 221, 189)$ physical points in the x, y and z directions – approximately 6 million degrees of freedom (though this could have been reduced substantially by decoupling velocity and density as for the direct solver). After omitting dealiased modes this corresponds to maximum Fourier wavenumbers of 39 in x, 61 in z and 110 collocation points in the half-channel $y \in (-1, 0)$. Obtaining a fully stratified state with the direct solver at these resolutions would be infeasible due to memory constraints. A Newton step at this resolution required approximately 6 hours of wall-clock time.

Appendix B. Streamwise-invariance of the high-*Pr* boundary layer

A steady passive scalar layer of thickness ϵ at the wall in (incompressible) plane Couette flow must be streamwise-invariant to leading order. To show that this is true we assume the opposite

and reach a contradiction. Substituting the asymptotic expansions of Eqs. (3.5*a*)–(3.5*c*) into the steady form of Eq. (2.1*c*) and presuming $\partial_x \rho_{PS} = O(\epsilon^0)$ leads to the dominant balance

$$-\frac{\partial \rho_{PS}}{\partial x} = \frac{1}{\epsilon^2 RePr} \frac{\partial^2 \rho_{PS}}{\partial Y^2}.$$

(B 1)

Taking a Fourier transform of Eq. (B 1) in x yields $-ik_x \epsilon^2 RePr \tilde{\rho}_{PS} = \partial_{YY} \tilde{\rho}_{PS}$ for a given streamwise wavenumber k_x, where $\tilde{\rho}_{PS}(k_x, Y, z, t)$ is the transformed density field. At any particular z, this has the general solution

$$\tilde{\rho}_{PS}(k_x; Y, z, t) = C_1 e^{Y\sqrt{-ik_x \eta}} + C_2 e^{-Y\sqrt{-ik_x \eta}}$$

(B 2)

for constants C_1 and C_2 and $\eta := \epsilon^2 RePr$. For the density field not to blow up in the interior, $C_1 = 0$, leaving just C_2 to be determined. Since the density boundary condition at the wall has no streamwise variation, $\tilde{\rho}_{PS}(k_x; 0, z, t) = 0$ for any $k_x \neq 0$. Consequently, C_2 also has to vanish meaning that ρ_{PS} has no streamwise variation, which is a contradiction.

REFERENCES

BUDANUR, N. B., SHORT, K. Y., FARAZMAND, M., WILLIS, A. P & CVITANOVIĆ, P. 2017 Relative periodic orbits form the backbone of turbulent pipe flow. *J. Fluid Mech.* **833**, 274–301.

CAULFIELD, C. P. & PELTIER, W. R. 2003 Mixing efficiency in stratified shear flows. *Annu. Rev. Fluid Mech.* **35**, 135–167.

CHANDLER, G. J. & KERSWELL, R. R. 2013 Invariant recurrent solutions embedded in a turbulent two-dimensional Kolmogorov flow. *J. Fluid Mech.* **722**, 554–595.

CHILDRESS, S. 1979 Alpha-effect in flux ropes and sheets. *Phys. Earth Planet. In.* **20**, 172–180.

CHILDRESS, S. & GILBERT, A. D. 1995 Stretch, twist and fold: the fast dynamo. *Springer* **37**.

CVITANOVIĆ, P. & GIBSON, J. F. 2010 Geometry of the turbulence in wall-bounded shear flows: periodic orbits. *Phys. Scr.* **2010** (T142), 014007.

DEGUCHI, K. 2017 Scaling of small vortices in stably stratified shear flows. *J. Fluid Mech.* **821**, 582–594.

DEGUCHI, K. & WALTON, A. G. 2013 A swirling spiral wave solution in pipe flow. *J. Fluid Mech.* **737**.

DUGUET, Y., BRANDT, L. & LARSSON, B. R. J. 2010 Towards minimal perturbations in transitional plane Couette flow. *Phys. Rev. E* **82** (2), 026316.

EAVES, T. S. & CAULFIELD, C. P. 2015 Disruption of SSP/VWI states by a stable stratification. *J. Fluid Mech.* **784**, 548–564.

ECKHARDT, B., SCHNEIDER, T. M., HOF, B. & WESTERWEEL, J. 2007 Turbulence transition in pipe flow. *Annu. Rev. Fluid Mech.* **39**, 447–468.

GARAUD, P., GAGNIER, D. & VERHOEVEN, J. 2017 Turbulent transport by diffusive stratified shear flows: From local to global models. i. numerical simulations of a stratified plane Couette flow. *Astrophys. J.* **837** (2), 133.

GIBSON, J. F., HALCROW, J. & CVITANOVIĆ, P. 2008 Visualizing the geometry of state space in plane Couette flow. *J. Fluid Mech.* **611**, 107–130.

GIBSON, J. F., HALCROW, J. & CVITANOVIĆ, P. 2009 Equilibrium and travelling-wave solutions of plane Couette flow. *J. Fluid Mech.* **638**, 243–266.

GIBSON, J. F., REETZ, F., AZIMI, S., FERRARO, A., KREILOS, T., SCHROBSDORFF, H., FARANO, M., YESIL, A. F., SCHÜTZ, S. S., CULPO, M. & SCHNEIDER, T. M. 2019 Channelflow 2.0. In preparation, see https://www.channelflow.ch.

GREGG, M. C. 1980 Microstructure patches in the thermocline. *J. Phys. Oceanogr.* **10** (6), 915–943.

HALL, P. 2012 Vortex-wave interactions/self-sustained processes in high Prandtl number natural convection in a vertical channel with moving sidewalls. *Stud. Appl. Math.* **129** (1), 1–25.

HALL, P. & SHERWIN, S. 2010 Streamwise vortices in shear flows: harbingers of transition and the skeleton of coherent structures. *J. Fluid Mech.* **661**, 178–205.

HALL, P. & SMITH, F. T. 1991 On strongly nonlinear vortex/wave interactions in boundary-layer transition. *J. Fluid Mech.* **227**, 641–666.

HAMILTON, J. M., KIM, J. & WALEFFE, F. 1995 Regeneration mechanisms of near-wall turbulence structures. *J. Fluid Mech.* **287**, 317–348.

HOLFORD, J. M. & LINDEN, P. F. 1999 Turbulent mixing in a stratified fluid. *Dyn. Atmos. Oceans* **30**, 173–198.

ITANO, T. & GENERALIS, S. C. 2009 Hairpin vortex solution in planar Couette flow: a tapestry of knotted vortices. *Phys. Rev. Lett.* **102** (11), 114501.

ITANO, T. & TOH, S. 2001 The dynamics of bursting process in wall turbulence. *J. Phys. Soc. Jpn.* **70** (3), 703–716.

KADER, B. A. 1981 Temperature and concentration profiles in fully turbulent boundary layers. *Int. J. Heat Mass Tran.* **24** (9), 1541–1544.

KAWAHARA, G., UHLMANN, M. & VAN VEEN, L. 2012 The significance of simple invariant solutions in turbulent flows. *Annu. Rev. Fluid Mech.* **44**, 203–225.

KERSWELL, R. R. 2005 Recent progress in understanding the transition to turbulence in a pipe. *Nonlinearity* **18** (6), R17.

KERSWELL, R. R. & TUTTY, O. R. 2007 Recurrence of travelling waves in transitional pipe flow. *J. Fluid Mech.* **584**, 69–102.

LIGNIÈRES, F. 1999 The small-Péclet-number approximation in stellar radiative zones. *Astron. Astrophys.* **248**, 933–939.

LINDEN, P. F. 1979 Mixing in stratified fluids. *Gephys. Astrophys. Fluid Dyn.* **13**, 3–23.

LUCAS, D. & CAULFIELD, C. P. 2017 Irreversible mixing by unstable periodic orbits in buoyancy dominated stratified turbulence. *J. Fluid Mech.* **832**, R1.

LUCAS, D., CAULFIELD, C. P. & KERSWELL, R. R. 2017 Layer formation in horizontally forced stratified turbulence: connecting exact coherent structures to linear instabilities. *J. Fluid Mech.* **832**, 409–437.

LUCAS, D., CAULFIELD, C. P. & KERSWELL, R. R. 2018 Layer formation and relaminarisation in plane Couette flow with spanwise stratification. *arXiv preprint arXiv:1808.01178* .

LUCAS, D. & KERSWELL, R. R. 2015 Recurrent flow analysis in spatiotemporally chaotic 2-dimensional Kolmogorov flow. *Phys. Fluids* **27** (4), 045106.

MELLIBOVSKY, F., MESEGUER, A., SCHNEIDER, T. M. & ECKHARDT, B. 2009 Transition in localized pipe flow turbulence. *Phys. Rev. Lett.* **103** (5), 054502.

MUNK, W. H. 1966 Abyssal recipes. *Deep-Sea Res.* **13** (4), 707 – 730.

OGLETHORPE, R. L. F., CAULFIELD, C. P. & WOODS, A. W. 2013 Spontaneous layering in stratified turbulent Taylor-Couette flow. *J. Fluid Mech.* **721**, R3.

OLVERA, D. & KERSWELL, R. R. 2017 Exact coherent structures in stably stratified plane Couette flow. *J. Fluid Mech.* **826**, 583–614.

PAPAVASSILIOU, D. V. & HANRATTY, T. J. 1997 Transport of a passive scalar in a turbulent channel flow. *Int. J. Heat Mass Tran.* **40** (6), 1303–1311.

PARK, Y.-G., WHITEHEAD, J. A. & GNANADESKIAN, A. 1994 Turbulent mixing in stratified fluids: layer formation and energetics. *J. Fluid Mech.* **279**, 279–311.

PRAT, V., GUILET, J., VIALLET, M. & MÜLLER, E. 2016 Shear mixing in stellar radiative zones—ii. robustness of numerical simulations. *Astron. Astrophys.* **592**, A59.

PRAT, V. & LIGNIÈRES, F. 2013 Turbulent transport in radiative zones of stars. *Astron. Astrophys.* **551**, L3.

PRINGLE, C. C. T., WILLIS, A. P. & KERSWELL, R. R. 2012 Minimal seeds for shear flow turbulence: using nonlinear transient growth to touch the edge of chaos. *J. Fluid Mech.* **702**, 415–443.

RUDDICK, B. R., MCDOUGALL, T. J. & TURNER, J. S. 1989 The formation of layers in a uniformly stirred density gradient. *Deep-Sea Res.* **36** (4), 597–609.

SCHLICHTING, H. & GERSTEN, K. 2016 *Boundary-layer theory*. Springer.

SCHNEIDER, T. M., ECKHARDT, B. & YORKE, J. A. 2007 Turbulence transition and the edge of chaos in pipe flow. *Phys. Rev. Lett.* **99** (3), 034502.

SCHNEIDER, T. M., MARINC, D. & ECKHARDT, B. 2010 Localized edge states nucleate turbulence in extended plane Couette cells. *J. Fluid Mech.* **646**, 441–451.

SKUFCA, J. D., YORKE, J. A. & ECKHARDT, B. 2006 Edge of chaos in a parallel shear flow. *Phys. Rev. Lett.* **96** (17), 174101.

SMITH, F. T. & BODONYI, R. J. 1982 Amplitude-dependent neutral modes in the Hagen-Poiseuille flow through a circular pipe. *P. Roy. Soc. A-Math. Phy.* pp. 463–489.

SURI, B., TITHOF, J., GRIGORIEV, R. O. & SCHATZ, M. F. 2017 Forecasting fluid flows using the geometry of turbulence. *Phys. Rev. Lett.* **118** (11), 114501.

SURI, B., TITHOF, J., GRIGORIEV, R. O. & SCHATZ, M. F. 2018 Unstable equilibria and invariant manifolds in quasi-two-dimensional Kolmogorov-like flow. *Phys. Rev. E* **98** (2), 023105.

SUTHERLAND, B. R., ACHATZ, U., CAULFIELD, C. P. & KLYMAK, J. M. 2019 Recent progress in modeling imbalance in the atmosphere and the ocean. *Phys. Rev. Fluids* **4**, 010501.

THORPE, S. A. 2016 Layers and internal waves in uniformly stratified fluids stirred by vertical grids. *J. Fluid Mech.* **793**, 380–413.

TUCKERMAN, L. S. 1989 Steady-state solving via Stokes preconditioning; recursion relations for elliptic operators. In *11th International Conference on Numerical Methods in Fluid Dynamics*, pp. 573–577. Springer.

TUCKERMAN, L. S., LANGHAM, J. & WILLIS, A. 2019 Order-of-magnitude speedup for steady states and traveling waves via Stokes preconditioning in Channelflow and Openpipeflow. In *Computational Modelling of Bifurcations and Instabilities in Fluid Dynamics*, pp. 3–31. Springer.

TURNER, J. S. 1973 *Buoyancy effects in fluids*. Cambridge University Press.

VISWANATH, D. 2007 Recurrent motions within plane Couette turbulence. *J. Fluid Mech.* **580**, 339–358.

VISWANATH, D. & CVITANOVIĆ, P. 2009 Stable manifolds and the transition to turbulence in pipe flow. *J. Fluid Mech.* **627**, 215–233.

WALEFFE, F. 1997 On a self-sustaining process in shear flows. *Phys. Fluids* **9** (4), 883–900.

WILLIS, A. P., CVITANOVIĆ, P. & AVILA, M. 2013 Revealing the state space of turbulent pipe flow by symmetry reduction. *Journal of Fluid Mechanics* **721**, 514–540.

ZAHN, J.-P. 1992 Circulation and turbulence in rotating stars. *Astron. Astrophys.* **265**, 115–132.

ZHOU, Q., TAYLOR, J. R. & CAULFIELD, C. P. 2017*a* Self-similar mixing in stratified plane Couette flow for varying Prandtl number. *J. Fluid Mech.* **820**, 86–120.

ZHOU, Q., TAYLOR, J. R., CAULFIELD, C. P. & LINDEN, P. F. 2017*b* Diapycnal mixing in layered stratified plane Couette flow quantified in a tracer-based coordinate. *J. Fluid Mech.* **823**, 198–229.